DEUTSCHES ELEKTRONEN – SYNCHROTRON
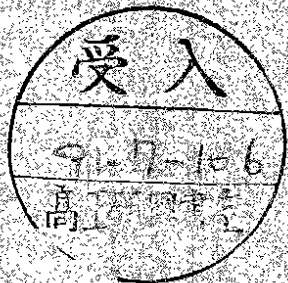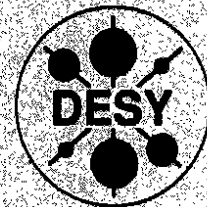
受入

91-Ⅱ-106
高エネルギー

Construction and Beam Test of the ZEUS Forward and Rear Calorimeter

ZEUS Collaboration

NOTKESTRASSE 85 · D - 2000 HAMBURG 52

To be sure that your preprints are promptly included in the
HIGH ENERGY PHYSICS INDEX,
send them to the following (if possible by air mail):

DESY
Bibliothek
Notkestrasse 85
D—2000 Hamburg 52
Germany

CONSTRUCTION AND BEAM TEST OF THE ZEUS FORWARD AND REAR CALORIMETER

The ZEUS Calorimeter Group

A.Andresen[1], A.Bamberger[2], A.Bargende[3], F.Barreiro[4], U.Behrens[5], S.Bentvelsen[6], M.Brkic[7], B.Burow[7], A.Caldwell[8], G.Cases[4], J.A.Crittenden[3], A.Dake[6], A.Dannemann[5], J.Dawson[9], K.Dierks[10], G.Drews[10], J.Engelen[6], H.Fawcett[11], W.Frisken[11], A.Fürtjes[10], D.Gilkinson[12], L.Hagge[10], R.Hamatsu[13], D.Hanna[12], J.Hartmann[3], T.Hasegawa[14], D.Hasell[11], M.Hazumi[14], L.Hervás[4], E.Hilger[3], U.Holm[5], T.Ishii[14], P.deJong[6], H.Kammerlocher[5], S.Kasai[14], S.Kitamura[13], R.Klanner[10], P.Kooijman[6], U.Kötz[10], M.Krämer[3], B.Krebs[5], W.Kröger[1], J.Krüger[1], M.Kuze[14], G.Levman[7], T.Lindenberg[2], H.vd Lugt[6], J.Martin[7], J.Mayer[16], J.Mitchell[12], P.Patel[12], T.Poser[2], K.Prange[3], S.Ritz[8], M.Rohde[10], T.Romanowski[15], E.Ros[1], H.-L.Schneider[3], D.Schäcke[2], W.Schulz[10], F.Selonke[10], W.Sippach[8], G.Smith[16], G.Stairs[7], J.Straver[6], G.Theisen[2], H.Tiecke[6], K.Tokushuku[14], B.Tröndle[2], T.Tsurugai[1], H.Uijterwaal[6], R.Ullmann[2], W.Vogel[10], K.Wick[5], T.Woeniger[1], S.Yamada[14], C.Youngman[10]

Abstract

The forward and rear calorimeters of the ZEUS experiment are made of 48 modules with maximum active dimensions of 4.6 m height, 0.2 m width, 7 λ depth and maximum weight of 12 t. It consists of 1 X_0 uranium plates interleaved with plastic scintillator tiles read out via wavelength shifters and photomultipliers. The mechanical construction, the achieved tolerances as well as the optical and electronics readout are described. Ten of these modules have been tested with electrons, hadrons and muons in the momentum range 15 - 100 GeV/c. Results on resolution, uniformity and calibration are presented. Our main result is the achieved calibration accuracy of about 1% obtained by using the signal from the uranium radioactivity.

1. INTRODUCTION

The measurements of neutral and charged currents and in particular the kinematical reconstruction of events via the determination of the variables x and Q^2, impose severe constraints on calorimetry for experiments at HERA [1]. A good calorimeter for such experiments is expected to be hermetic, provide excellent energy resolution and good angular resolution for jets as well as sufficient electron to hadron discrimination. In order to fulfil these requirements, the ZEUS Collaboration [2] has proposed and constructed a uranium-scintillator calorimeter. This type of calorimeter has been demonstrated to provide an optimum energy resolution for single hadrons of $35\%/\sqrt{E}$ (E in GeV) and at the same time compensation, that is, equal response for electrons and hadrons (e/h=1) [3]. The choice of scintillator readout with photomultipliers offers additional advantages: the pulses are shorter than the bunch-crossing time of 96 ns so pile-up effects are avoided, a time resolution for pulses of a few ns can be achieved, this being important to reject an estimated cosmic background of 5 kHz, a modular construction is possible and, finally, the noise can be kept at a low level.

The ZEUS Collaboration has performed several tests in order to confirm that compensation and an energy resolution of $35\%/\sqrt{E}$ for single hadrons can be achieved with uranium-scintillator calorimeters [4]. Realistic prototype modules have been constructed in order to check the mechanical design and performance of the calorimeter with respect to uniformity and calibration [5], response to low energy particles [6] and to jets [7]. The results obtained showed that the uranium natural radioactivity can be used as a powerful tool for calibration [5]. It ensures for these prototype modules an intercalibration of individual calorimeter sections to about 3% and a stability of calibration to better than 1%.

In this article we describe the construction of ZEUS forward and rear calorimeter modules and the test of ten of them in a beam with electrons, muons and hadrons in the momentum range of 15 to 100 GeV/c. We show that, due to a strict quality control on the module components and assembly, a section-to-section intercalibration accuracy close to 1% and a long term monitoring of this calibration to better than 0.5% can be achieved for these final modules by means of the uranium radioactivity alone. The performance of final electronics and a preliminary version of the readout system to be used for the ZEUS calorimeter are also presented.

2. CALORIMETER STRUCTURE

2.1 Overview of the ZEUS Calorimeter.

The ZEUS high resolution calorimeter surrounds the solenoid and tracking detectors hermetically, as shown in fig.1. The solid angle coverage is 99.8% in the forward hemisphere and 99.5% in the rear hemisphere. Mechanically the calorimeter divides into 3 main components:
- the forward calorimeter (FCAL) covering polar angles from $\theta = 2.2^0$ to 39.9^0.
- the barrel calorimeter (BCAL) extending from $\theta = 36.7^0$ to 129.2^0.
- the rear calorimeter (RCAL) extending from $\theta = 128.1^0$ to 176.5^0.

The structure of the 3 calorimeter components is similar. They are subdivided longitudinally into 2 parts. The inner part constitutes the electromagnetic calorimeter (EMC) with a depth of about 25 radiation lengths (X_0) or 1 interaction length (λ) for hadronic interac-

[1] Univ. of Hamburg, II.Inst.for Exp.Phys., FRG (supported by BMFT)
[2] Univ. of Freiburg, FRG (supported by BMFT)
[3] Univ. of Bonn, FRG (supported by BMFT)
[4] Univ. Autónoma de Madrid, Spain (supported by CAICYT)
[5] Univ. of Hamburg, I.Inst.for Exp.Phys., FRG (supported by BMFT)
[6] NIKHEF-H, Amsterdam, The Netherlands
[7] Univ. of Toronto, Canada (supported by NSERC)
[8] Columbia Univ., USA (supported by NSF)
[9] Argonne National Lab., USA (supported by DOE)
[10] DESY, Hamburg, FRG
[11] York Univ., Canada (supported by NSERC)
[12] McGill Univ., Canada (supported by NSERC)
[13] Tokyo Metropolitan Univ., Japan
[14] INS, Univ. of Tokyo, Japan
[15] Ohio State Univ., USA (supported by DOE)
[16] Univ. of Manitoba, Canada (supported by NSERC)

Typeset by $\mathcal{A}_{\mathcal{M}}\mathcal{S}$-TEX

tions. The outer part is called the hadronic calorimeter (HAC). It varies in depth from 6 λ in the very forward region to about 3 λ in the rear region. In both FCAL and BCAL the HAC is read out in 2 sections (HAC1 and HAC2). The planes of division are non-projective for FCAL and HAC2. For BCAL, both EMC and HAC are projective in azimuthal angle (ϕ) but only the EMC is projective in θ. The basic dimension for the cell readout in the transverse direction is 20×20 cm^2 for HAC sections of both FCAL and RCAL. The EMC calorimeter is further segmented into 5×20 cm^2 and 10×20 cm^2 sections for FCAL and RCAL respectively. Each calorimeter section is read out on both sides (right and left) by wavelength shifter plates (WLS), light guides (LG) and photomultipliers (PM). In order to improve the electron-hadron discrimination power of the calorimeter, two layers of 3×3 cm^2 wide silicon detectors are foreseen inside the electromagnetic calorimeter of FCAL after 3 and 6 X_0. For BCAL and RCAL, only one layer is foreseen after 3 X_0.

The sampling thickness for both EMC and HAC has been chosen to be 1 X_0, leading to depleted uranium (DU) plates 3.3 mm thick. The DU plates are fully encapsulated by a stainless steel foil of 0.2 mm thickness in the EMC and 0.4 mm in the HAC. The steel foil allows a safe handling of the uranium plates during construction and at the same time its thickness serves to adjust the signal from the DU natural radioactivity. This signal has to be low enough to keep the photomultiplier background current and the noise small, but still high enough to provide an accurate calibration. The scintillator (SCI) thickness has been chosen to be 2.6 mm in order to achieve e/h=1, according to previous measurements [3,4]. The layer structure of the calorimeter is detailed in tables 1a and 1b for EMC and HAC sections respectively.

The calorimeter has a modular structure. Each FCAL/RCAL module has a width of 20 cm and a height for the active part varying from 2.2 to 4.6 m, depending on its position with respect to the beam. Fig. 2a and 2b show front views of FCAL and RCAL respectively. In the region where the F/RCAL is hidden behind the barrel, the EMC segmentation is identical to the one in the HAC, namely 20×20 cm^2 (these sections are called HAC0 sections). Both FCAL and RCAL consist of 24 modules including 2 special modules to be positioned above and below the beampipe. Tables 2a and 2b present an inventory of all different types of FCAL and RCAL modules.

2.2 Module structure

Module description. From the mechanical point of view the main components of a module are (see fig.3):
- a steel C-frame which provides the overall mechanical module structure.
- a stack of depleted uranium plates and scintillator tiles,
- spacers between DU plates,
- wavelength shifter plates mounted in cassettes for the readout of the scintillator light,
- stainless steel straps which compress the stack and fix it to the C-frame,
- shielding structure consisting of back-beam of the C-frame and two layers of pipes and
- PMs with high voltage (HV) bases mounted in the shield.

In addition each module houses a bundle of optical fibers and a bundle of small pipes which guide a radioactive source, used for calibration purposes, as explained later.

The C-frame. Fig.4a shows a sketch of the C-frame. The dimensions given refer to the largest FCAL modules. The C-frame has three main components: the end-beam, the upper C-leg and the lower C-leg. The end-beam is made of the following parts (fig.4b): front-plate, web-plate, two end-plates and lower plate. The lower plate is only present during the assembly and the transport of the module and is removed once the module is installed in the experiment.

The end-beam supports the stack of scintillator and DU-plates during assembly and transport. The mechanical tolerances are very stringent, in particular front-plate and web-plate are straight to within 0.5 mm over their full length. Every 20 centimeters a 'bulkhead' is screwed to the web-plate (fig.4b) with the function of guiding the DU weight to the web and also to fix the stainless steel straps which compress the DU/scintillator stack. The web-plate has a hole pattern repeated every 20 cm for the attaching of photomultiplier housings.

The upper and lower C-legs are bolted to the end-beam. The DU-plates are fixed to the C-legs by means of clamps. Both C-legs have to be mounted within a fraction of a millimeter parallel to each other and perpendicular to the front-plate of the end-beam. Via the upper C-leg there is access to the optical fibers and source tubes. The upper C-leg serves also to house the electronics for the readout of the silicon detectors. Once the module is installed in the experiment, it is positioned such that it rests completely on the lower C-leg. Both C-legs are made of normal steel plates welded into box beam profiles. For the lower C-leg the plate thickness is 25 mm, for the upper C-leg it is only 10 mm at the locations where the electronics is mounted and 20 mm elsewhere. The cross-sections are 158×197 mm^2 and 353×197 mm^2 for lower and upper C-legs, respectively.

DU plates. The bare DU-plates are produced at MSC[1] in Oak Ridge (USA). The material composition[2] is 98.1% ^{238}U, 1.7% Nb and less than 0.2% ^{235}U, the density being about 18.9 g/cm^3. The radiation length for pure ^{238}U is 3.2 mm and the nuclear interaction length is 10.5 cm. The plate width is 188.8 ± 0.25 mm for the EMC section, 183.8 ± 0.25 mm for the HAC1 section and 178.8 ± 0.25 mm for the HAC2 section. The nominal plate thickness, 3.3 mm, is measured at the production site every 20 cm along the edge. The plates for EMC sections are selected with a mechanical tolerance in any of these thickness measurements of ±0.15 mm. Those failing this criterion are recut for HAC sections. In the same way the thickness tolerance for HAC1 plates is ±0.20 mm and for HAC2 plates is ±0.25 mm. Fig. 5a to 5e show distribution of these thickness measurements for plates of the various calorimeter sections. We note that the r.m.s. thickness is around 2%. Since production methods limit the maximum length of a plate to about 3 m, it was necessary to weld two plates together to produce lengths up to 4.6 m as required for the largest modules. The weight of such a plate is about 55 kg.

All plates are clad with a stainless steel foil, 0.2 mm thick for the EMC plates and 0.4 mm for the HAC plates. The nominal cladding tolerances are ±10 μm. They have been monitored by recording the thickness with 2 μm accuracy at the rolling mill using chart recorders and this information has been used to accept the material. The r.m.s. of the thickness distribution is estimated to be about 5 μm for the 0.2 mm thick foil. The seam of the foil is laser welded at the side of the plate, over the full length. The stainless steel end pieces are also welded to

a good uniformity, a decay time suitable for the readout through PMs in between HERA bunch crossings, sufficient radiation hardness towards the HERA background and the exposure to uranium radioactivity and, last but not least, a non-prohibitive cost. The choice was SCSN-38[1], a cast polystyrene material doped with 1% p-PBD and 0.02% BDB fluors [9]. The stability of SCSN-38 light yield and attenuation length against radiation damage was investigated extensively at high, medium and low dose rates [10] and proved to be adequate for the anticipated HERA background conditions, about 100 Gy/year close to the beam-pipe in addition to about 10 Gy/year from the uranium radioactivity. The long time behaviour and the effect of low dose rate irradiation of scintillator by DU plates are shown in fig.8a and 8b. Fig.8a shows the change in attenuation length of a 5 mm thick piece of SCSN-38, sandwiched between two DU plates. The observed decrease in attenuation length after 500 days of irradiation and an absorbed dose of 14.3 Gy is the same as for a non-irradiated piece, thus indicating that the effect is caused by normal aging rather than by the irradiation itself. Fig.8b shows identical measurements during a longer period (1079 days and an absorbed dose of 52 Gy) for a 2.6 mm thick scintillator piece. Here some initial difference is observed between the irradiated and the non-irradiated sample, but in both cases the attenuation length converges with time to a constant and nearly identical value.

The response of a calorimeter to electrons and hadrons depends on the relation between scintillator response L and specific energy loss dE/dx. According to [11] it can be described by a semi-empirical formula

$$\frac{dL}{dx} \propto \frac{dE}{dx}\left(\frac{1}{1+kB \cdot dE/dx}\right)$$

where kB is the Birks' parameter. Using electrons and protons, the following value for the Birks' parameter has been measured [12]:

$$kB(SCSN-38) = (0.842 \pm 0.015) \cdot 10^{-2} \text{ g/cm}^2/\text{MeV}.$$

The nominal lateral dimensions of FCAL scintillator tiles are shown in fig.9. The scintillator plates delivered by the manufacturer were cut on a precision disk saw. All edges were polished to optical quality by machining them on a diamond lathe. The cut-outs for the spacers remained unpolished. Dimensions of the processed pieces were constantly checked in order to achieve a maximum lateral tolerance of 0.2 mm. The manufacturer provided a thickness measurement over a grid of points for each plate, identified via oriented bar code labels. Only plates in the thickness range of 2.6±0.2 mm were accepted. The plates were grouped according to their mean thickness and flatness and, via a computer-controlled process, a selection for EMC, HAC1 and HAC2 sections was performed. EMC plates were selected from the center of the two-dimensional thickness-flatness distribution and HAC1 plates from the center of the remaining distribution. After cutting and polishing, each scintillator piece, identified by a bar code label, was weighed and this information recorded on an IBM-PC. From this weight measurement and the exact dimensions, it is possible to deduce the thickness distribution of the scintillator pieces, shown in fig.10a to 10d. For EMC and HAC1 sections

[1] Product of Kuraray Co.,Ltd., Tokyo (Japan).

the cladding. The mechanical connection between the plates and the C-legs is made via these end-pieces. After the welding and cladding[1] the plates are subjected to the following acceptance criteria for width: 189.8±0.25 mm, 184.8±0.25 mm and 179.8±0.25 mm respectively for the EMC, HAC1 and HAC2 plates. The plates were requested to be straight to within 0.5 mm over the full length, while the length itself must be precise to ±0.2 mm up to the maximum plate length of 4.6 m.

Spacers. The DU plates are separated from each other by spacers to avoid pressure on the scintillator. They are located along the edge of the DU-plate every 20 cm (fig.6). From the physics point of view, spacers and the corresponding cut-outs in the scintillator should be as small as possible, to avoid signal losses. On the other hand the size of the spacer should be sufficient to support the weight of the stack and the tensioning force exerted by the straps, which press the whole stack onto the end-beam. The spacers are normally 3.9 mm thick. In HAC sections their cross-section is 5×10 mm². For EMC sections their cross-section is 5×10 mm². They are made of tungsten carbide and fabricated using powder metallurgy[2]. Their cross-section can be reduced to 5×6 mm² because they have to carry the weight of a smaller number of DU-plates.

Stainless steel straps. Fig.7a shows the cross-section of a whole stack. Near the top of the stack, after 3 and 6X₀, a 15 mm gap is left free for installation of silicon detectors. The top plate is a 15 mm thick aluminium plate with edges rounded off to allow the stainless steel straps to slide easily over the top in order to balance the force at both sides. The DU/scintillator stack is compressed by means of these steel straps, 196 mm wide and 0.25 mm thick, one per tower. They also keep the WLS cassettes in position. The straps compress the stack with a force of 15-20 kN per tower, which implies a compression of about 3 mm. The straps are fixed below the front plate of the end-beam via the bulkheads to the photomultiplier housing assembly, as sketched in fig.7b.

Finite Element Calculations. Finite element techniques have been used to calculate the forces and stresses which act in a module under transport conditions, during installation and after installation under the influence of the magnetic field. From these calculations one derives the minimum spacer dimensions, the forces acting on the spacers and, finally, the minimal strap tension needed to avoid any movement of the spacers. Several models have been used. An extensive description of the results can be found in [8]. These calculations have shown for example that an additional external steel frame is required to reinforce the C-frame during transport and handling operations and that a strap tension of 15-20 kN is required. The modules have been designed to stand in the transport position (which is also the stacking position) vertical accelerations up to 4 g and horizontal accelerations up to 1 g.

2.3 Optical readout

Scintillator. The scintillator material was selected to fulfil the following criteria: maximum and uniform light yield, attenuation length in excess of the cell dimensions to obtain

[1] Chalk River Nuclear Laboratories (Canada)
[2] Kennametal (Canada)

of FCAL an additional sorting of pieces was performed in order to avoid systematic effects due to the positioning of the pieces inside the stack.

To protect the scintillator surface from mechanical damage and to enhance and uniformize the light yield, the pieces were wrapped in white Tyvek paper (quality 1073D from Du Pont) whose reflectivity matches that of aluminum foil. On the inside of the Tyvek paper a correction pattern consisting of black stripes was printed to improve the readout uniformity throughout the scintillator surface. These patterns were optimized according to the scintillator dimensions for the construction of the prototype modules [5]. The resulting uniformity is ±2.5% after combining the light output from both readout edges. Fig.11a, b and c show respectively a pattern used for FCAL-EMC sections and uniformity measurements performed before and after uniformity correction.

Wavelength shifters. The transport of light from the scintillator to the PMs is performed via WLS plates as shown in fig.12a and 12b. The WLS material selected was Y7 in PMMA[1] base with an ultraviolet absorbant for wavelengths below 360 nm [9]. This material has an absorption spectrum which matches well the emission spectrum of SCSN-38 and, compared to the dye K27, provides a more uniform readout and 10% more light yield. The emission spectrum of Y7 is well matched to the spectral absorption of the PM photocathodes. Other properties of this WLS material are long attenuation length, hardness against aging and radiation [10] and easy machining (sawing, bending, polishing, gluing). WLS and LG were made of a single plate in order to avoid light losses in the glue joints and also to improve the uniformity in the sensitive region. The thickness of WLS plates was 2.0±0.2 mm and the concentration of the Y7 dye was 30 ppm for HAC sections and 45 ppm for the shorter EMC sections. The concentration of Y7 was optimized in order to achieve a good uniformity, which requires a low concentration, and at the same time high light yield, which requires a high concentration[2].

An optimum uniformity of response was achieved by 'end reflectors', to reflect the light at the face opposite to the PM, and 'back reflectors' to reflect the light on the side opposite to the scintillator (fig.12a). These reflectors were made of aluminized mylar foils or Tyvek paper with, for the back reflector, a printed pattern made of black dots. The pattern has been determined separately for each WLS bar by measuring its response under computer control. After printing the pattern the uniformity has been verified. Fig.13a and 13b show respectively the uniformity of a WLS plate for a HAC1 section of FCAL before and after correction with reflectors. The inhomogeneity is reduced typically from 12% to 3%, well within specifications [13].

In total nearly 7000 plates of 18 different types were produced. The main difficulty in the production of WLS was to maintain the high quality polishing of the edges, especially important for EMC sections of FCAL, in order to achieve the required light yield. The cutting, polishing, bending and gluing of the LG end-strips, which finally have to match the PM photocathode was also a time and effort consuming task. After machining, all WLS plates were tempered to reduce mechanical stresses and avoid cracks and the non-active areas were covered by protective paper. The WLS plates corresponding to the right or left side readout

[1] Product of Kuraray Co.Ltd. Tokyo (Japan).
[2] For a given WLS thickness of 2 mm. PMMA doped with 45 ppm absorbs more than 60% of the scintillator light and allows the compensation of non-uniformities up to 20%, while material doped with 30 ppm allows the compensation of non-uniformities up to 30%.

of one complete tower were mounted into 0.2 mm thick stainless steel cassettes (see fig.12b). The cassette includes two brass pipes 2.5 mm in diameter (only 1 for RCAL) between EMC plates, where radioactive sources can be moved (see section 2.5). Mechanical contact between scintillator and WLS is avoided by 0.3 mm thick nylon fishing lines. This ensures that optical coupling is uniform over the entire surface.

Strict quality control was performed all along the production cycle. The composition and spectral transmission of the material was controlled by the manufacturer. All plates were labelled and a selection was performed on the basis of thickness mappings. The back reflector patterns were determined according to the plate dimensions on the basis of uniformity measurements performed with a xenon lamp. After assembly inside the cassettes, a final check was performed and the information on light yield and uniformity recorded in a data base. Fig.14a and 14b show the result obtained for the most important and critical EMC plates of FCAL. This result is well within the specifications.

Photomultipliers. The requirements on PMs are good gain stability, good linearity over the entire dynamic range and small dark current. Based on of extensive measurements on prototype samples, the XP1911 tube from Philips was selected for EMC sections of FCAL and the R580 tube from Hamamatsu Photonics for all other sections. Both PMs are 10-stage head-on tubes with diameters of 19 and 38 mm respectively. They have bi-alkaline photocathodes with a spectral response well suited to match the spectrum of the Y7 WLS. The PMs have been equipped with bases containing a Cockcroft-Walton (CW) generator to supply the HV. Such bases[1], produced by Matsusada[2] according to the ZEUS design, have the advantage of:
- total power dissipation of 170 mW, which is one order of magnitude smaller than for usual resistive bases,
- simple control and safe operation as the maximum external voltage is only 24 V,
- good voltage stability for anode loads up to 50 μA,
- PM protection due to current limitation at 75 μA and
- elimination of the bulk and expense of HV distribution cables.

The main difficulties of this design are the quantized voltage steps[3], the need to suppress the switching noise and the small dimensions.

All PMs were tested with the corresponding CW base and selected for installation in the calorimeter. The test cycle consisted of a burn-in period followed by measurements of dark current, gain, linearity, long term stability and stability versus average anode current. These measurements were performed in two test facilities (DESY and INS) where 120 and 80 PMs, respectively, could be tested at once. The first test facility used LED sources for pulsed light and a tungsten lamp for DC light, complemented with a laser for linearity measurements. The second test facility employed a xenon lamp for pulsed light. The PMs were selected on the basis of the following criteria:
- quantum efficiency of at least 12% at 520 nm,
- dark current smaller than 1 nA for XP1911 and 3 nA for R580,
- linearity of response within ± 2% up to anode charges of 2000 pC, corresponding to a peak

[1] To our knowledge the use of high frequency CW bases for HV supply was pioneered by L.Babbeling around 1980 for the NA-11 experiment at CERN.
[2] Matsusada Precision Devices Inc. (Japan).
[3] 17 steps and 22 steps were applied for R580s and XP1911s, respectively.

current of 100 mA for pulses with 20 ns half-width,
- stability of response better than 1% up to 1 s and better than 3% up to 4 hours and
- stability of response better than 5% for an anode current change from 0.1 to 10 μA.
All these measurements were performed at nominal gain (gain times quantum efficiency of
5·10⁴) and for anode currents produced by DC light in the range of 0.1 to 10 μA. In total
about 2500 XP1911 and 4800 R580 tubes were tested. Especially critical for calibration
is the requirement on small dark current. Fig.15a and 15b show for XP1911 and R580
PMs, respectively, the distribution of the dark current measured at nominal gain and at
a temperature of 25⁰C. It peaks at about 0.1 nA with very few PMs failing the selection
criterion. The dark current has the following temperature dependence:

$$I_d = I_0 \cdot \exp(T/T_0) \qquad (T \text{ in } {}^0C)$$

with a temperature parameter T_0 of 8 to 10⁰C, implying the rise by almost a factor 2 in case
where T increases from 25 to 30⁰C. Even then, most of the PMs would fulfil the specifications
on the dark current level. The typical temperature dependence of the gain times quantum
efficiency product is +0.25%/⁰C and −0.05%/⁰C for XP1911 and R580 PMs, respectively.

2.4 Stacking

The modules were assembled at NIKHEF (Netherlands) and York University (Canada).
The largest FCAL modules each contain 185 DU plates, 5980 scintillator tiles, 9024 spacers
and 46 wavelength shifter cassettes. A great effort was made during assembly to position all
these components with high accuracy, in order to minimize module-to-module differences. For
this reason, and also to minimize the human exposure to uranium radioactivity, the assembly
process was performed by a computer control using a commercial robot at NIKHEF (see
fig.16a) and a custom built stacking machine in Canada.

The NIKHEF stacking robot could pick up uranium plates and complete layers of scin-
tillator tiles and spacers by vacuum suction, and move them in 3 dimensions via computer
controlled motors. Each motor shaft was equipped with a rotation angle encoder in order
to measure x, y and z coordinates. This robot could lift weights up to 180 kg. The various
movements to be executed by the robot were programmed and downloaded when necessary
from a PC to the control computer.

Each module assembly started with the positioning of the C-frame, followed by mounting
of bulkheads, fiber bundles and source tubes on the web-plate of the end-beam. The frame
had to be aligned to 0.1 mm with respect to the robot, leveled and attached to the floor. A
table was positioned on each side of the stacking robot, one containing a box with uranium
plates and the other the scintillator tiles and spacers aligned on a template. The exact
position of these tables was measured by sensors read out by the PC and introduced in the
'stacking program' which could then proceed with limited human intervention.

The Canadian stacking procedure was somewhat different in detail. The C-legs were not
attached to the module until after stacking. This allowed for precision guides to be used to
control the position of the DU plate via their precisely cut end pieces and the scintillator
layers via similar end pieces on the scintillator vacuum lift. Pairs of guides along the length

of the stacking machine constrained the DU plates and straightened the stack to ±0.5 mm.
This allowed bowed DU plates (up to 3 mm) to be used. These guides moved vertically
upward as stacking proceeded. As at NIKHEF, the stacking was fully automatic apart from
placing each layers of scintillator pieces and spacers on the template.

An important parameter to control during stacking was the module height in each tower.
The variations in height were caused by thickness tolerances of the uranium plates. Every 25
DU−SCI layers, the stack was compressed and its height measured by digital linear displace-
ment sensors read out by the PC. These measurements, along with thickness measurements
for each DU plate available in a large data-base, were then used to calculate the correction
to be applied to the next 25 layers via the spacers. which were available in 3 thicknesses:
3.8, 3.9 (nominal) and 4.0 mm. In this way the height of EMC, HAC1 and HAC2 sections
never deviated from nominal value by more than 1 mm. Fig.16b shows a typical example of
measured deviations from nominal height for a completely stacked module.

When the stacking was completed, including the front aluminum plate, the straps were
mounted and tensioned to the proper value, between 15 and 20 kN, after which the plates
were clamped to the C-legs. The straps were then removed one after the other in order to
introduce the WLS cassettes and PM housings and to connect light fibers and source tubes.
After these operations the straps were positioned and tensioned again. In order to prevent
deflection of the module, a support iron frame was attached to it for crane lift and transport.
More details about module stacking can be found in [14].

2.5 Calibration tools

The nuclei of uranium ${}^{238}_{92}U$ decay in 3 steps into ${}^{234}_{92}U$ nuclei, by emitting α, β and γ rays
[15] as shown in fig.17a. The nuclei of ${}^{234}_{92}U$ are not stable and decay further into ${}^{206}_{82}Pb$ via
11 steps (7 α and 4 β decays). However the lifetime of these nuclei is long enough so these
additional decays do not contribute to the signal observed in the scintillator (UNO signal).
The α particles (4.2 MeV) carry most of the energy in the decay process (about 80%) but
they have a range in uranium of only 7 μm. They are therefore stopped either in the DU
plate or in the cladding and do not contribute to the signal observed in the scintillator. The β
particles carry about 20% of the energy and their maximum energy is 2.3 MeV (Pa→U decay)
corresponding to a range of nearly 1 mm in uranium. The γ rays (about 1% of the energy)
result from the decay of excited isotopes to the ground state and have a spectrum in the
region of 10 to 1000 keV. The composition of the DU radioactivity has also been measured at
the surface of 3 mm thick plates [15]. The result is 2600 counts/(cm².s) for β particles above
10 keV, with an average energy of 200 keV, and 442 counts/(cm².s) for γ rays above 60 keV,
with an average energy of 500 keV. These measurements indicate that the DU radioactivity
at the surface of the plate is still dominated by very low energy electrons and is therefore
very sensitive to the cladding thickness. In fact, using absorption dose measurements [16],
we estimate a signal reduction of about 70% after 0.2 mm of iron and of about 90% after 0.4
mm (see next section).

Since the lifetime of uranium nuclei is 4.5·10⁹ years, the uranium natural radioactivity
provides an extremely stable signal for calibration purposes. Assuming an uranium density of
19 g/cm³, one expects 3.5·10⁴ decays per cm² per second, that is, 1 decay every 10 ns in the

smallest sections of the calorimeter (EMC sections of FCAL). This signal can be integrated and measured as a DC current (UNO current) by the front-end electronics (see section 3.4). It amounts to 100 nA for EMC sections of FCAL at nominal PM gain (see section 4.2). The UNO current can be used not only to monitor the PM gain, but also to intercalibrate calorimeter sections which are geometrically identical. Finally it can be used as a reference in order to transport the absolute calibration scale obtained in a test beam. The uranium radioactivity is complemented by the following calibration tools (see fig.17b): movable γ sources, light flashers (LED and lasers) and charge injectors.

The movable γ sources [17] consist of encapsulated pointlike samples of Co^{60} with an activity of 2.0 mCi which can be pushed by a motor driven steel wire through the brass pipes described in section 2.3. They provide local information on the calorimeter structure which is complementary to the information provided by the uranium radioactivity, uniformly spread over the sections. In particular they allow the detection of stacking errors like shifted or shadowed scintillator layers or a mismatch between the scintillator and the wavelength shifter cassette. They also allow measurements on the uniformity of light collection along the WLS and of light attenuation in the scintillator. Finally they will provide information on the change of attenuation length of the optical components due to aging or radiation damage by comparing measurements performed regularly inside the ZEUS detector.

The light flasher system [18] consists of a dye laser pumped by a nitrogen laser to provide light which is distributed to all PMs. The distribution of light is accomplished in two stages. Primary distribution occurs at the output of the laser where the light is distributed into 50 m long silica fibers which run into the calorimeter. Secondary distribution occurs in the upper C-leg of each module where the light from the incoming fibers is distributed to each PM by PMMA fibers of equal length. The light flasher can be used to check the complete readout chain from the PM onwards, to determine the linearity of the system up to the highest expected signals, to perform a timing of all channels and finally to determine the photoelectron yield.

The charge injectors are coupled to each front-end card as described in section 3.4. They are used to check the readout chain from the front-end electronics onwards and to balance the gain of all electronic channels (note that the UNO current follows a different path than normal AC signals, as explained in 3.4).

2.6 Influence of tolerances in calibration

In this section we estimate the effect of scintillator, uranium and cladding thickness tolerances in the calorimeter calibration assuming this calibration is performed using the uranium radioactivity. The electron sampling fraction can be written as follows:

$$\epsilon = \left(\frac{\epsilon}{mip}\right) \frac{\epsilon_s s}{\epsilon_u u + \epsilon_c c + \epsilon_s s}$$

e/mip being the ratio between the sampling fraction of electrons and the sampling fraction of minimum ionizing particles[1], u, c, s refer to nominal uranium, cladding and scintillator

---

[1] This ratio is rather independent of uranium, scintillator and cladding thicknesses. Its value is about 0.62 for the ZEUS calorimeter.
The sampling fractions for electrons and mips are respectively 4% and 6.6%

sampling thicknesses (namely 3.3, 2×0.2 and 2.6 mm) and ϵ_u, ϵ_c, ϵ_s to the corresponding dE/dx losses (20.7, 11.7 and 2.0 MeV/cm respectively). Therefore the effect of thickness variations Δs, Δu, Δc, on the electron response is:

$$\frac{\Delta\epsilon}{\epsilon} = f_s^e \frac{\Delta s}{s} + f_u^e \frac{\Delta u}{u} + f_c^e \frac{\Delta c}{c}$$

with $f_s^e = 0.93$, $f_u^e=-0.87$ and $f_c^e=-0.06$ for the EMC calorimeter sections. For many calorimeter layers and assuming no correlation between layer tolerances we obtain:

$$\frac{\Delta\epsilon}{\epsilon} = F_s^e \frac{\Delta s}{s} \oplus F_u^e \frac{\Delta u}{u} \oplus F_c^e \frac{\Delta c}{c}$$

where Δs, Δu and Δc are now r.m.s. thickness fluctuations and the coefficients are:

$$F_s^e = \left[\sum_i (f_s^e \epsilon_i)^2\right]^{1/2}$$

Similar expressions hold for F_u^e and F_c^e. The coefficients ϵ_i are the fraction of energy deposited by electrons in each layer and the sum runs over all layers inside a section (26 for the EMC case).

As the calorimeter is calibrated using the uranium radioactivity, the important quantity for calibration is the ratio e/UNO, UNO being the uranium radioactivity signal measured in the corresponding section. To evaluate the effect of tolerances in the UNO signal we have used the results from [16]. According to these measurements, the radiation dose rate of a thick uranium plate behind an absorber of thickness t can be parametrized by:

$$Dose(t) \sim Ae^{-t/a} + Be^{-t/b}$$

where A and B are material independent quantities ($A \approx 1.95$ mGy/h and $B \approx 0.05$ mGy/h) whereas a and b scale approximately with dE/dx losses. In particular $a_s= 1.24$ mm and $b_s= 36$ mm for scintillator and $a_c= 0.17$ mm and $b_c=6.5$ mm for iron. The first term in the dose parametrization can be viewed as the short range component of the uranium radioactivity (β component) and the second term as the long range component (γ component). The energy absorbed by a scintillator layer of thickness s located behind an iron sheet of thickness c is therefore:

$$UNO \sim Ac^{-c/a_c}a_s(1 − e^{-s/a_s}) + Be^{-c/b_c}b_s(1 − e^{-s/b_s})$$

This formula is simply an integration over the scintillator thickness of the dose remaining after the cladding. The effect of thickness variations in the UNO signal for single layers is therefore:

$$\frac{\Delta(UNO)}{UNO} = f_s^{uno} \frac{\Delta s}{s} + f_c^{uno} \frac{\Delta c}{c}$$

with $f_s^{uno}= 0.40$ and $f_c^{uno}=-0.99$ for EMC sections. The effect of the uranium plate thickness in the UNO signal is much smaller, we estimate $f_u^{uno} \sim 0.05$. In the same way as for the electron sampling fraction, the effect of thickness tolerances on e/UNO for complete EMC sections of the calorimeter can be calculated by summing over all 26 layers:

$$\frac{\Delta(e/UNO)}{e/UNO} = F_s \frac{\Delta s}{s} \oplus F_u \frac{\Delta u}{u} \oplus F_c \frac{\Delta c}{c}$$

with $$F_s = \left[\sum_i (f_s^\epsilon \epsilon_i - f_s^{uno} \epsilon_{uno})^2\right]^{1/2}$$

Similar expressions hold for F_u and F_c. The quantity ϵ_{uno} is the fraction of the UNO signal contributed by a single layer. The F coefficients are rather energy independent. At 10 GeV we obtain $F_s = 0.21$, $F_u = 0.25$ and $F_c = 0.18$. Taking into account the thickness tolerances referred in previous sections, 1.1% for scintillator, 1.9% for uranium and 1.8% for cladding (2 sheets per layer), we expect $\Delta(e/UNO) \approx 0.6\%$ (see table 3a), the largest contribution coming from the uranium plates.

We have estimated in the same way $\Delta(h/UNO)$ and $\Delta(\mu/UNO)$ for EMC and HAC sections of the calorimeter, h being the sampling fraction for hadrons and μ the mean response for muons. The main differences between EMC and HAC sections are the number of layers (80 instead of 26) and the cladding thickness (0.4 instead of 0.2 mm). The tolerances are also slightly looser for HAC but the signal is more spread inside the section (in fact we have assumed flat distributions for ϵ_i in the case of muons and hadrons). The results are presented in tables 3b to 3e. We obtain for EMC(HAC) sections $\Delta(h/UNO)\sim 0.4\%(0.3\%)$ and $\Delta(\mu/UNO)\sim 0.3\%(0.2\%)$, dominated by the cladding.

For an experimental determination of $\Delta(e/UNO)$, $\Delta(h/UNO)$ and $\Delta(\mu/UNO)$ we refer to the results of the beam test in chapter 5. Comparing the thickness measurements on the mechanical components to the mean particle response allows to verify some of the input numbers (f_j) of this study. A significant correlation has been found between the measured DU plate thickness and the e/UNO ratio in the EMC sections of FCAL and RCAL [19]:

$$\frac{\Delta(e/UNO)}{e/UNO} = -(0.75 \pm 0.30)$$

compatible with the expected ratio:

$$\frac{\Delta(e/UNO)}{e/UNO} = f_u^\epsilon + f_u^{uno} = -0.87 + 0.05 = -0.82.$$

As this is only one of many contributions to the $\Delta(e/UNO)$ spread, correction for this correlation reduces the experimental spread of $\Delta(e/UNO)$ by about 8% only.

3. EXPERIMENTAL SETUP

3.1 Beam setup

The X5 test beam of the CERN-SPS was used to calibrate the modules. This tertiary beam was produced by particles resulting from 120 GeV/c π^- interactions with Be, Cu or Pb targets. Acceptable beam rates of negatively charged particles could be obtained in the range of 10 to 110 GeV/c. At 15 GeV/c the beam contained almost exclusively electrons and at 100 GeV/c, a 50% electron-50% muon beam was obtained with the Pb target and a 30% hadron-70% muon beam with the Cu target, after removing the electrons with a 5 mm Pb absorber placed at the intermediate focus.

The trigger system (see fig.18a) consisted of a coincidence between 4 scintillation counters. The 6 mm wide B3 counter was used to define the incident beam position. The counter B4,

with a 3 cm diameter hole in the middle, was used to veto beam halo particles. No event selection was performed at the trigger level since sufficient discrimination between the different particle types was provided by the calorimeter itself at the energies used for calibration.

The deviation of the beam momentum from its nominal value was measured for each event by a spectrometer described in the next section. The momentum spread depended on the opening of a horizontal collimator located just upstream of the spectrometer. Typically an opening of ±10 mm was used for electron runs corresponding to a momentum spread with r.m.s. of 1%. For hadron runs ±25 mm was used in order to enrich the hadron content of the beam relative to muons, resulting in a proportionally larger momentum spread. The beam intensity was typically below 20000 particles per spill (spill length≈ 2.4 seconds) except for the energy scan runs (40000 particles per spill due to the larger collimator opening).

3.2 Beam momentum determination

The beam optics (see fig.18b) were implemented with two dipole-magnet strings and five quadrupole magnets. These optics produced a horizontal dispersive focus at a distance of 80 m from the production target and vertical and horizontal non-dispersive foci at a distance of 190 m where the calorimeter modules were installed. The momentum-analyzing dipole magnets deflected the beam in the horizontal plane. Horizontal and vertical collimators at the position of the first focal point limited the beam cross section directly upstream of the beam spectrometer described below. Thus situated at a dispersive focus, the horizontal collimator also defined the momentum distribution of the beam. The particle rates downstream of the collimator were proportional to its setting for slit widths of less than 50 mm. During electron calibration runs the collimator opening was set to ± 10 mm.

The momentum of each particle incident on the calorimeter modules was measured in a magnetic spectrometer located 100 m upstream of the modules. Fig.18c depicts the geometrical arrangement of the spectrometer, which consisted of four planes of proportional chambers positioned symmetrically about a string of four dipole magnets. The calculation of particle momentum proceeds in two steps:

1- The momentum of a particle following the nominal trajectory (bend angle: 37.48 mrad) was derived from magnetic field measurements performed by previous users of the beam [20]. This derivation uses the recorded readback value of the magnet current and a correction for the relationship between the recorded readback current and the current measured at the magnet. The uncertainty in the absolute value of the field integral was estimated to be 0.3%. The readback currents were stable to less than 0.1 A during the entire period of calibration. The ratio of true to nominal beam momentum is plotted versus beam momentum in fig.18d.

2- The reconstruction of the trajectory of each particle permitted the determination of the deviation of the magnetic deflection Θ from its nominal value and hence of the relative deviation from the momentum determined in step 1. A local scintillator trigger permitted the latching of the proportional chamber data in the readout electronics located near the chambers. A request signal furnished by the ZEUS fast trigger electronics caused the data to be inserted into the data stream via a CAMAC link. The dead-time inherent in the buffering of the spectrometer data resulted in an inefficiency of 5 - 10% for the beam fluxes

typical during the calibration (about 10 kHz). The chamber efficiencies were such as to permit momentum reconstruction in 85 - 95% of the events for which the chamber data were available. The exact calculation of the relative momentum deviation as a function of the four hit positions x_i (in units of mm) is given by

$$\frac{P - P_{true}}{P_{true}} = \frac{\Theta - \Theta_{true}}{\Theta_{true}} = -\left[\frac{1}{0.03748}\right]\left[\frac{(x_4 - x_3)}{7270} - \frac{(r_2 - x_1)}{7305}\right]$$

The survey alignment uncertainty of 0.5 mm per chamber implies a 0.8% uncertainty in the absolute momentum scale determination.

3.3 Slow control

The complete DAQ system is shown schematically in fig.19a. The movement of the module under test and the HV setting for the PMs were performed by the slow control tasks, implemented in a 68020 microprocessor running under the OS9 operating system. This computer could be accessed by the main computer, a MicroVAX 3600, via an Ethernet link as explained in 3.5.

All modules were tested in the horizontal position (see fig.19b). They were bolted to a support which could be moved by remote control from the 68020 computer in both the vertical and the horizontal directions. The position of the support was measured with linear and rotational shaft encoders with a precision better than 0.5 mm in both directions. Moving the module was achieved by reading continuously the coordinates and switching off the driving motor at the demanded position. Since the breaking path varied along the support rails, a target position could only be reached within 2 to 3 millimeters in a single try. This precision was sufficient for the measurements performed.

The HV of the PMs was controlled by 16-channel CAMAC controllers which could supply the low voltage to the CW generators implemented in the bases and read the monitoring voltage as well. Each controller included a 12-bit DAC to supply the voltage and a 12-bit ADC to read the monitoring voltage. A VME version will be used for operation in the ZEUS experiment.

3.4 Readout electronics

The 96 ns crossing time of electrons and protons at HERA and the expected high background rates require a complex trigger scheme. A parallel pipelining of the data and the first level trigger provides the necessary processing time of 5 μs. The pipelined calorimeter readout electronics has to fulfil the following requirements:
- a dynamic range equivalent to 16.5 bits allowing precise energy measurements from mips (300 MeV equivalent energy in EMC sections of FCAL) up to the highest expected signals (about 400 GeV in individual sections of FCAL),
- a timing of calorimeter signals with precision of a few ns in order to reject the cosmic background and beam-gas events.

In addition, the quasi DC current in the PMs produced by the uranium natural radioactivity has to be measured with a precision better than 1% for calibration purposes. The

fluctuations of this current (uranium noise) set an upper limit to the electronic noise, which should not dominate the total noise. The solution adopted for the readout electronics is a shaping-sampling-pipelining scheme [21] which is briefly described below.

The PM signals are integrated and shaped such that the rise and fall times are longer than the 96 ns crossing time. This pulse is then sampled in steps of 96 ns (see fig.20a) and the samples stored for digitization. The signal sampling and storage is performed via an analog pipeline based on the switched capacitor technique. The pipelines, with 58 cells each, have been developed in collaboration with the Fraunhofer Institute[1] using CMOS technology. Events selected by the trigger can be picked inside the pipeline and transferred to a buffer of similar design. Pipelines and buffers are incorporated in the so-called 'front-end cards'. A preliminary version of this electronics, implemented however with CCDs as pipelines, was successfully tested with the prototype calorimeter [6].

The modules tested in the beam were equipped with front-end (analog) cards of the final FCAL design. These cards were attached to a removable beam located on top of the module so that the same cards were used to read out all modules. In total 22 cards were used, each one containing the readout for 12 channels. Right (R) and left (L) side PMs were connected to different cards. The signal of each PM is split into 4 parts (see fig.20b). The quasi DC current produced by the uranium radioactivity is measured via a current to voltage converter using a feed-back resistor R_M with some smoothing by a capacitor (integration time of 20 ms). The remaining three parts are AC-coupled via resistive splitting into:
- the 'high-gain' path (H) with shaper, pipeline (58 cells) and analog buffer (8 cells) to store 8 samples for each pulse,
- the 'low-gain' path (L) identical to the 'high gain' path but scaled down by a factor 22.22 and finally
- the trigger path, not used in the beam test described here.

The 'high gain' path covered the range between 0 and 20 GeV/c and the 'low gain' path up to about 400 GeV/c. This signal splitting allowed to reach the effective dynamic range of 16.5 bits required by the specifications. In order to meet the requirements concerning calibration the R_M resistors employed for DC current integration were selected with a tolerance of 0.1% and all other sensitive components of the front-end card with 1% tolerance. In addition, each card incorporated a calibration system consisting of a 10-bit DAC allowing charge injection to all channels and a 2 V reference voltage precise to within 0.1% (see fig.20b).

The analog signals processed by the front-end cards were transmitted via 60 m long flat twisted-pair cables to the digital cards. These VME-based digital cards contained a 12 bit ADC with a conversion rate of 1 MHz. The final version of the digital card incorporates a DSP[2], in order to extract from the pulse samples the energy and time information as described in section 4.3. In the test presented here these operations were performed offline. Each digital card could read out 12 channels, the information from one channel including 8 samples for H and L gain respectively, in addition to the UNO current. Since only 3 of these cards were available at the time of the test, only 36 channels could be read out per event, corresponding (in the case of FCAL modules) to 3 complete calorimeter towers. The selection of the 3 towers to be read out for a given run was performed via a computer-controlled multiplexer unit.

3.5 Data acquisition

The data acquisition system (DAQ) had the following major tasks: provide a stable and flexible environment for data taking in the test beam, test the computing hardware used by the ZEUS experiment and provide experience with software tools.

The DAQ system consisted of three subsystems implemented in different computing devices as follows (see also fig.19a):
- host functions, interface to beam and test triggers and run-control in a MicroVAX 3600 with 16 MB RAM, about 900 MB disk space and two 1600 BPI tape drives,
- generating triggers and readout of ADCs by two T800 transputers [22], each one with 1 MB private RAM and 128 kB dual ported RAM for VME access and
- slow control by a single VME board computer with a 68020 microprocessor running under OS9.

The MicroVAX acted as host computer. The transputers were connected to it by a 20 Mbit serial link and the OS9 machine via Ethernet using TCP/IP. The slow control operations have already been described in section 3.3. The readout tasks were implemented in the transputers. One of them was used to control the front-end electronics, react on VME interrupts and read out the VME-ADCs and CAMAC crates (e.g. trigger counters and beam spectrometer). The data block was then transferred to the second transputer and was formatted into ZEBRA[1] data banks. The records obtained in this way were then buffered and transferred to the MicroVAX in blocks of 36 to 40 kB. The event data, as well as the data delivered by the OS9 computer, were buffered in the VAX using MBM[2] and were there available for storage on disk or data quality monitoring (DQM). This DQM was implemented using the histogram package PAW[3].

Data taking was initiated and controlled by a task implemented in the VAX. This task could start, control and stop a run by sending commands to the transputers in order to set the trigger conditions, and also to the OS9 system in order to control the position of the module. A run, formed by consecutive events with the same trigger conditions and slow control setting, was stored in a single file of the VAX disk prior to writing to tape. In addition, a feature called 'autopilot' was available to perform a sequence of runs with changing parameters, like the scan of a module with the beam or a calibration cycle of all calorimeter towers with UNO, charge injection, laser or LED runs (see section 4.2). The data were finally copied from disk to tape in ZEBRA exchange format.

The event rate achieved within this scheme was mainly limited by the MicroVAX computer. With an event size of about 1600 bytes, the transfer rate from the transputers to the VAX was 160 kB/s. The rate for the transfer to disk was 84 kB/s. Taking into account the spill structure of the SPS (2.4 s long spills followed by a pause of 12 s) the event rate was limited to a maximum of about 300 Hz or 700 events per spill.

[1] Data structure management system from the CERN ECP Division
[2] Model Buffer Manager from the CERN ECP Division
[3] Physics Analysis Workstation from CERN ECP Division

4. TEST PROCEDURE

4.1 Warm-up procedure

In total, 6 of the 24 FCAL modules and 4 of the 24 RCAL modules were tested in the X5 test beam of the CERN SPS. These modules will be called in the following FCAL1 to FCAL6 and RCAL1 to RCAL4. They were all of maximum-size type (4.6 m height) and consisted of 23 20×20 cm^2 towers. Module FCAL5 was of the F11 type (see table 2a) and all other FCAL modules of the F12 type. Modules RCAL2 and RCAL4 were of type R11 (see table 2b) and the 2 others of the type R12.

The module to be tested in the beam was first rotated to the horizontal position and installed on a warm-up stand where PMs and HV distribution boards were mounted. A preliminary HV adjustment was performed by balancing the UNO currents measured via current-voltage converters. The module was kept under HV for a few days and various tests were performed (e.g. light tightness, gain stability tests and voltage dependence of the PM gain).

This warm-up stand was also used to scan the modules with radioactive sources. A pointlike Co^{60} source (length 1 mm and diameter 0.7 mm) with an activity of 2 mCi was moved along the brass pipes located in between the WLS plates as described in section 2.4. The source was encapsulated at the end of a 10 m wire and was moved with a speed of 4-5 mm/s by a driver mechanism based on pinch rollers driven by computer-controlled stepper motors[1]. Measurements were taken at a rate of 10 Hz, ensuring 2-3 points per mm, that is, about 20 points per calorimeter layer. The time separation between measurements, 100 msec, was longer than the integration time for the UNO current (20 msec). The source scans produced a signal in excess of the UNO value by 60% for HAC sections and by 150% for EMC sections. Fig.21a and 21b display the result of EMC and HAC scans, respectively. The ripple observed reveals the layer structure of the calorimeter and allows the position and light yield of individual scintillator tiles to be checked. The two large dips observed in the EMC scan correspond to the position of the gaps to be instrumented with silicon detectors. The Co^{60} source scans turned out to be a powerful method for the detection of small local mistakes in the module. More details about these measurements can be found in [17].

4.2 Beam test procedure

The module to be tested was transported by crane from the warm-up stand to the beam calibration stand and cabled up to the front-end cards. The final HV settings were tuned such that the UNO currents deviated by less than 1% from the following nominal values :
- 100 nA for FEMC channels,
- 200 nA for REMC channels,
- 400 nA for FHAC0 and RHAC0 channels,
- 500 nA for FHAC1, FHAC2 and RHAC1 channels.

The pipeline and buffer cells of every channel were calibrated using a test voltage applied at the input of the pipelines (see table 4a) and various laser and LED measurements were performed. Measurements of the UNO pedestals and noise studies were also performed at

[1] The slow control computer was used for these measurements.

a reduced HV value of 400 V. The vertical (x) and horizontal (y) position of the module with respect to the beam were determined with an accuracy of about ±1 mm and ±3 mm, respectively. by scanning the center of tower 12 in both directions with a 15 GeV/c electron beam (see fig.22a and 22b).

The beam test of a module consisted of 4 'beam-on' scans (see table 4b) at 15 and 100 GeV/c and horizontal (y) position of the module could be reached by particle signals. The first scan (15 GeV/c electrons incident at the center of each HAC0 and EMC section) was repeated at the end of the cycle in order to check the reproducibility of the calibration. In each scan the calorimeter was automatically moved to the desired position via the autopilot procedure incorporated in the run control. Histograms of mean values and spread of the average calorimeter response at the center of each section were available from the online monitoring at the end of each scan. These scans were complemented with other measurements, e.g. scans at ±6 cm vertically displaced from the center of the module, in order to determine the attenuation of the light in the scintillator, and fine step scans in small regions of the calorimeter. The duration of each scan was typically 8 hours for FCAL modules and 4 hours for RCAL modules.

Between two 'beam-on' scans, a 'beam-off' calibration cycle was performed. This cycle consisted of 7 (4) calorimeter scans for FCAL (RCAL) modules, one per multiplexer setting, in order to monitor the performance of PMs and electronics (see table 4c). The cycle started with a measurement of the UNO currents followed by asynchronous charge injection runs (to determine the gain of the electronics), random triggers (to check noise and pedestals) and finally various light injection runs. The 'beam-off' cycles lasted typically 1 hour. The complete test of one module, including mechanical operations, took on average 1 week with however large variation from module to module.

4.3 Charge and time reconstruction

In this section we describe the sequence of operations required to extract the charge and time information. Fig. 20a shows the PM pulse after the shaper. As the input pulse was much shorter than the shaping time constant, the pulse shape is to a very good approximation identical for all events and channels. This pulse was sampled every 96 ns and the samples stored in the pipeline cells. Upon receipt of a trigger, 8 samples h_i, chosen so that the pulse peaked between the third and the fourth sample[1] were stored in the buffer cells and transferred to the ADCs for digitization. These samples were corrected off-line as follows:

$$H_i = \frac{g_p g_b}{g_0}[h_i - \delta_0 - \delta_p - \delta_b] \qquad (i = 0,...7)$$

where g_0 and δ_0 are a global gain and pedestal and $g_p, g_b, \delta_p, \delta_b$ are small corrections which depend on the pipeline and buffer cells in which the signal was stored. These constants were determined by applying a known test voltage at the input of the pipelines (see fig.20b and table 4a). The charge q (in pC) was obtained from the samples H_i (in ADC channels) by the

[1] The electronics was run in asynchronous mode (relative to the particle arrival time) in the test beam. At HERA the sampling clock will be synchronised with the bunch crossings so these two samples are equal for all events. This time is defined in the following as T=0.

19

following algorithm:

$$q = q_{norm}[(H_2 - H_0) + R_q(H_3 - H_0)]$$

where $R_q = -(dH/dt)_2/(dH/dt)_3$ is the ratio of slopes between samples 2 and 3 determined at the time such that $H_2 = H_3$ (this time is defined as T=0). The same value of R_q was used for all channels ($R_q = 1.80$). The normalization factor q_{norm} includes various ADC to pC conversion factors and a global channel gain correction obtained by injecting known test charges into the shaper via the capacitor C_R (see fig.20b). In order to ensure that the same charge is injected in each channel, the capacitor C_R was trimmed beforehand to better than 0.2% with a variable capacitor C_V. The applied voltage V_{DAC} was monitored event by event relative to a precise 2 V reference voltage V_{REF}.

The charge q required several further corrections:

$$Q = q/R_1 - \Delta P$$

where $R_1 = I_{uno}(measured)/I_{uno}(nominal)$ is a correction for variations in the PM gain obtained from the measured UNO current and ΔP is a global channel pedestal determined from random trigger runs without beam. The charge obtained in this way depends on the time at which the event occured relative to the sampling clock (see fig.23a) and therefore needs an additional time correction :

$$Q_{corr} = Q/(1 + \sum_{i=1}^{4} a_i T_c^i)$$

where $T_c = T_0 + \Delta T$, T_0 being the overall time of the event as determined by the trigger-pipeline clock time difference and ΔT the shift for individual channels. This shift is due to the transit time of the PM and in the pipeline and may be as big as 10 to 20 ns. The polynomial coefficients a_i depend on the pulse type (beam, Q injection, LED, laser). The same values can be used for all channels. The time shifts ΔT, on the contrary, depend on the pulse type and also on the channel.

The time of each event was reconstructed from the shaped pulse itself via the following algorithm:

$$T = (H_2 - H_3)/(S_q \cdot Q) \qquad (T = 0 \text{ for } H_2 = H_3)$$

where $S_q = [(dH/dt)_2 - (dH/dt)_3]/Q$. For T in ns, S_q has the value 0.81 (the same value was used for all channels). Just as in the case of the reconstructed charge Q, this time T needs a time correction for asynchronous events (see fig.23b):

$$T_{corr} = -\Delta T - \sum_{i=1}^{4} b_i T^i$$

where ΔT is the time shift introduced previously to correct the channel to channel time offsets. In the following, the corrected charge and time, Q_{corr} and T_{corr} will be simply called Q and T.

Finally the UNO current was determined as follows (see fig.20b):

$$I_{uno} = (V_{uno} - V_G)/R_M - I_0$$

20

where V_{uno} is the UNO signal and V_G the reference ground. Both are measured event by event. R_M is the value of the integrator resistor (3.48 MΩ for FCAL cards of the final design) and I_0 a residual pedestal measured with the HV at 400 V.

In total 279 constants per channel are required in addition to 37 further constants common to all channels. No update of these constants was necessary during the calibration of one module except for the UNO current correction R_I which was updated approximately every 8 hours. Typical variations after one week of running were 0.3% (0.5%) for electronics H (L) gain, 0.03 pC (0.28 pC) for pedestals and 1.2% (0.7%) for UNO currents of EMC (HAC) channels. After 8 hours of running the UNO current variations were typically 0.5% (0.2%) for EMC (HAC) sections.

4.3 Effective integration gate

In electron showers the energy is deposited promptly. This is not the case for hadron showers, especially if a large fraction of the signal is due to neutron interactions as in uranium-scintillator calorimeters. As explained in [23] most of the neutrons produced in hadron showers are prompt but it takes a finite time until they are slowed down and deposit their energy by elastic collisions with the protons of the scintillator. Once the neutrons reach thermal energies the dominant process is the neutron capture by uranium nuclei with emission of γ rays in the MeV range. These photons start to contribute to the signal typically after 100 ns and therefore modify the e/h value for long integration gates. This decrease of e/h for long integration gates is confirmed by the experimental data (see [24] and references therein). Due to the finite decay time of scintillator and WLS. a prompt energy deposit in the calorimeter results in a finite-length pulse at the PM anode. Its shape is dominated by the decay constants of the WLS (about 9 ns for 99% of the light and 40 ns for the remaining 1%). As a result, a significant time dependence is observed both for the electron and the hadron signal for gate lengths below 100 ns.

In the test performed with the prototype calorimeter [5], the PM signals were digitized after 50 m RG-58 cables by charge integrating ADCs (2282B from LeCroy) with a gate length of 100 ns. In the following we discuss the weighting function of the present readout electronics and reconstruction algorithm. This function describes the contribution to the total signal of the energy deposited in the calorimeter at times different than the prompt energy. Since the shaper circuit performs 4 equal integrations with $\tau=33$ ns [21], its response to a δ-function pulse at t=0 with area Q is described by the function (see fig.20a):

$$h(t) = \frac{Q}{6\tau} \left(\frac{t}{\tau}\right)^3 e^{-t/\tau}$$

with $\tau=33$ ns. The signal shape of prompt energy deposits in the calorimeter has been determined using electrons incident on the calorimeter at arbitrary times relative to the sampling clock. It can be described to a good approximation by the same function $h(t)$ with just an increased time constant, $\tau=36.5 \pm 0.2$ ns, which reflects the signal delay due to geometrical effects, scintillator and WLS decay times and PM response. The reconstruction algorithm presented in the previous section results in the weighting function $\omega(T)$ given in fig.24a. T being the time relative to the prompt energy deposit in the scintillator, reconstructed with

weight $\omega=1$ at time T=0. After 110 ns this weight drops below 50% so for smooth pulse this electronics can be compared with an integrating ADC with a gate ending 110 ns after the mean arrival time. In the prototype measurements [5], the beginning of the gate was adjusted to start typically 20 ns earlier than the pulse, so the present electronics should be compared with integrating electronics of 130 ns gate length. As this value is similar to the one actually used, no significant differences regarding compensation are expected.

The sampling electronics are on the contrary very different from the integrating electronics for early pulses. Fig.24b shows the weighting function $\omega(T)$ also for negative values of T. We can see that for early signals one might even reconstruct a negative charge (due to the H_0 subtraction in order to obtain the correct baseline). This function is important for pile-up studies and noise calculations. In particular the uranium noise measured for the prototype [5] was 25 MeV per tower (EMC+HAC1+HAC2), almost a factor 2 smaller than for the present electronics (see section 5.6).

5. TEST RESULTS

5.1 Linearity

An electron energy scan in the momentum range of 15 to 110 GeV/c was performed for module FCAL1. The beam was incident at the center of section 2 in tower 13 (equipped with XP1911 PMs). The mean charge Q measured by the calorimeter for both high and low gain channels is plotted versus beam momentum in fig.25. This charge Q includes, in addition to the charge collected in the section of beam incidence, the charge collected in the high gain channels of adjacent EMC and HAC1 sections (R and L side channels are added). These adjacent sections contain approximately 10% of the total signal. Fig.25 shows that the high gain channel saturates at an energy of about 20 GeV/c.

The momentum of the incident particle was corrected event by event for deviations from the nominal value, using the beam spectrometer. The aperture of the horizontal collimator which defines the momentum spread was set to ±25 mm during this energy scan.

The deviation from linearity is defined as:

$$\delta = (Q/p)/(Q_0/p_0) - 1$$

where Q_0 and p_0 are the calorimeter charge and beam momentum at 15 GeV/c. Fig.26a displays δ versus beam momentum for the low gain measurements. We observe deviations from linearity smaller than 1% in the momentum range covered by the measurements.

The energy resolution obtained from the r.m.s. of the electron response is plotted versus beam momentum in fig.26b. At the lower measured momenta the resolution is about $17.5\%/\sqrt{E}$, compatible with previous measurements [5] and with measurements performed in the high gain of other channels and modules (see section 5.6). At the highest measured momenta the resolution degrades slightly to $19\%/\sqrt{E}$.

A similar scan was performed for module RCAL1 with the beam incident at the center of section 1 in tower 12 (equipped with R580 PMs). The quantity δ defined previously is plotted versus beam momentum in fig.27a and the energy resolution in fig.27b. We observe in this

case an increase in δ of about 2% between 15 and 110 GeV/c. This nonlinearity is consistent with measurements performed for other sections of FCAL and RCAL modules which are also equipped with R580 PMs (see next section). The beam test provides no information on the system linearity beyond 110 GeV/c. This information can be extracted from the laser data, reaching equivalent energies in excess of 400 GeV.

5.2 Test of the EMC sections

The EMC sections of the FCAL and RCAL modules were tested with 15 and 100 GeV electrons and with 100 GeV muons, incident at the center of each section (see table 4b). Electrons at 15 GeV were selected by demanding a signal between 110 and 180 pC in the EMC part of the calorimeter, but smaller than 15 pC in the hadronic part. Fig.28a shows the resulting distribution with high statistics, obtained by superimposing the events from all sections of one module. This distribution is to a good approximation a gaussian, whose mean and r.m.s. were calculated for each section (no fit was performed) and used in the present analysis. Electrons at 100 GeV were selected by demanding a signal between 800 and 1100 pC in the EMC sections, but smaller than 100 pC in the HAC sections. Muons were selected by demanding a signal between 1 and 40 pC in the EMC section exposed to the beam, but smaller than 120 pC in the total calorimeter. The resulting distribution, again with high statistics, is displayed in fig.28b. The muon pulse-height distribution is well described by the following function (also shown in the figure):

$$f(x) = f_0 \cdot \phi[(Q - Q_0)/\sigma]$$

where Q is the measured charge, ϕ the Landau distribution (see [25] and references therein) and f_0, Q_0, σ are free parameters which have been obtained for each section from the corresponding fit. An 'effective mean value' of the muon signal can be obtained using these fitted parameters, as follows:

$$Q_{mean} = \int_0^{Q_{max}} Q \cdot f(Q)dQ / \int_0^{Q_{max}} f(Q)dQ = \sigma \cdot \Phi_1(\lambda_{max}) + Q_0$$

where $\lambda_{max} = (Q_{max} - Q_0)/\sigma$ and $\Phi_1(x)$ is the first moment of the Landau distribution truncated at a value x, as defined in [25]:

$$\Phi_1(x) = \int_{-\infty}^{x} \lambda \cdot \phi(\lambda)d\lambda / \int_{-\infty}^{x} \phi(\lambda)d\lambda$$

This effective mean value has been used in the present analysis. It has the advantage over the arithmetic mean value of a smaller statistical error and less sensitivity to a hadron contamination of the muon samples and the value of Q_{max}.

Results concerning the test of EMC and HAC0 sections from the 6 FCAL and 4 RCAL modules are summarized in tables 5a and 5b. In all tables R and L side PM signals have been added. Table 5a shows, for electron and muon scans and for each module, the mean

---

1 This may be due to the quantized voltage steps in the CW base used for R580s

23

charge measured by each EMC section, averaged over all sections of the module. Averaging over all modules and over H and L gain, a charge of 142.6 pC is measured by the calorimeter for 15 GeV/c incident electrons (for each run all EMC sections from 3 towers[1] are summed; HAC sections are excluded but they contain only 0.2% of the signal at 15 GeV). This value sets the absolute calibration scale of the calorimeter for the UNO current value of 100 nA for EMC sections of FCAL. The module-to-module variations Δ are at the 0.5% level and the matching between H and L gain is accurate to 0.1%. This matching is also excellent for individual PMs (see fig.29a and 29b for FCAL and RCAL respectively). The intercalibration of H and L gain was obtained with charge injection. The area of the EMC sections of RCAL is exactly twice the corresponding area for FCAL. When setting $I_{UNO}(REMC) = 200$ nA and $I_{UNO}(FEMC) = 100$ nA we expect the same energy calibration. We find the following ratios FCAL/RCAL from table 5a:

$$15\,GeV/c : \quad \frac{e(FCAL)}{e(RCAL)} = \frac{142.6}{138.6} = 1.029,$$

$$100\,GeV/c : \quad \frac{e(FCAL)}{e(RCAL)} = \frac{951.6}{944.5} = 1.008,$$

$$100\,GeV/c : \quad \frac{\mu(FCAL)}{\mu(RCAL)} = \frac{4.74}{4.64} = 1.022 \quad \text{(corresponding to 500 MeV deposited energy).}$$

For the scaling between the 100 GeV/c and 15 GeV/c data we find:

$$FCAL : \quad \frac{e(100)}{e(15)}\frac{15}{100} = \frac{951.6}{142.6}\frac{15}{100} = 1.001,$$

$$RCAL : \quad \frac{e(100)}{e(15)}\frac{15}{100} = \frac{944.5}{138.6}\frac{15}{100} = 1.022,$$

consistent with the linearity measurements presented in the previous section. The nonlinearity of the RCAL thus appears to be the dominant cause of the response differences. Similar nonlinearities are found in the HAC0 section of both FCAL and RCAL. The difference in the average electron signal measured at 15 GeV/c between the HAC0 and the other EMC section of the module is 1.5% for the FCAL and 0.7% for the RCAL. We expect that the different types of PMs (XP1911 for the EMC sections of FCAL and R580 for all other sections) are the cause of the response difference. This is presently under detailed investigation using the laser calibration system.

As mentioned before, the 15 GeV/c electron scan was performed twice for each module, at the beginning and at the end of the calibration cycle, in order to check the reproducibility of the calibration. The values obtained in both scans for individual channels agree within the statistical error of 0.3 to 0.4%. Module FCAL3 was tested a second time, after 4 months. The values obtained in both tests agree within 0.4%, thus indicating that beam calibration constants are stable also in the long term.

The HV values were set as explained in section 4.2 and remained fixed during the test of a given module. A test was performed in one tower of module RCAL1 measuring e/UNO as a function of HV and hence of PM gain. The HV was varied over a range of 60 V around nominal value. The e/UNO values changed by less than 0.5% over this HV range which corresponds to a variation of 50% in PM gain.

---

1 In the case of FCAL modules, these 3 towers include 12.5×20 cm² EMC sections. The section on which the beam centered contains about 90% of the electron energy.

24

Table 5b shows the section-to-section spreads of e/UNO and μ/UNO within a given module. They are typically 1% for FCAL modules at 15 and 100 GeV/c and somewhat larger for RCAL modules. If all sections of all modules are put together, the spread of e/UNO is 1.1% (FCAL) and 1.5% (RCAL) as seen in fig.30a and 30b respectively. These values measure the calibration uncertainties for the case that the calibration is derived from the UNO currents alone.

In total 900 FCAL and 328 RCAL EMC channels have been tested in the beam, representing 36% and 23%, respectively, of the total number of FCAL and RCAL channels.

5.3 Test of the HAC sections

The HAC1 and HAC2 sections of FCAL and RCAL modules were tested with 100 GeV hadrons and muons incident at the center of each section (see table 4b). Muons at 100 GeV were selected by demanding a signal in the corresponding HAC section between 3 and 80 pC, but smaller than 120 pC in the whole calorimeter. Fig.31a and 31b show high statistics muon distributions in HAC1 and HAC2 sections of FCAL modules. These distributions are well described by the Landau function introduced for EMC sections and 'effective mean values' were calculated in exactly the same way. Hadrons at 100 GeV were selected by demanding a signal in EMC+HAC1 sections between 400 and 1000 pC, but smaller than 850 pC in EMC sections in order to reject electrons. In the cut used to select hadrons, HAC2 sections were omitted in order to perform a similar analysis for FCAL and RCAL modules. Due to this cut and also to incomplete containment of hadron showers in a single module, about 16% of the hadrons were rejected, mainly late showering particles. This cut affects of course the mean hadron values (they increase by about 12% in HAC1 sections) but not the section-to-section comparison, since the same cuts were applied to all sections. We also note that late showering hadrons contaminate the muon samples for RCAL modules, shifting slightly the mean values as discussed later. Fig.32a and 32b show high statistics hadron distributions in HAC1 and HAC2 sections of FCAL modules. The mean values of these distributions were calculated for each section and used in the present analysis.

The result of the various scans performed in the HAC sections is summarized in tables 6a and 6b. The module-to-module variations are of the order of 1% for both muons and hadrons except for module FCAL1, which shows significantly lower pulse-heights in both HAC1 and HAC2 sections for hadrons. If tower sums (EMC+HAC1+HAC2) are considered, there is no discrepancy for FCAL1. This effect is not understood up to now.

The ratio between the muon signal in HAC1 and HAC2 is:

$$\frac{\mu(HAC2)}{\mu(HAC1)} = \frac{15.64}{15.56} = 1.005.$$

The ratio values are at the expected level according to previous studies [5]. Compared to the FCAL, the RCAL HAC1 sections is 0.5% larger for muons and 2% smaller for hadrons. The first effect can be explained by hadron contamination of the muon RCAL sample, as commented before. The second effect can be explained by the fact that back-scattering from HAC2 into HAC1 sections is not possible for RCAL modules. A recalibration of RCAL HAC sections is therefore not implied by these effects.

The μ/UNO section-to-section spread (see table 6b and fig.33a and 33b) is of the order of 1%. The h/UNO spreads are larger. For HAC1 sections this is due to the problem in FCAL1 mentioned previously (see fig.34a). For HAC2 sections there is a large contribution from statistical fluctuations. However, if the total energy in the towers (EMC + HAC1 + HAC2) is considered, the variations are small, at the 1% level (see fig.34b). From these results we conclude that the UNO currents provide a calibration of HAC sections accurate to about 1%. Since a single module does not provide full containment for hadron showers, studies on e/h, energy resolution for hadrons or EMC/HAC intercalibration are not possible. These studies were performed in detail with the prototype calorimeter [5].

In total 552 FCAL and 184 RCAL HAC channels have been tested in the beam, representing 30% and 20%, respectively, of the total number of FCAL and RCAL channels.

5.4 Light yield of EMC sections

Sufficient light yield is important in order not to degrade the electron energy and position resolution. A value of 80 photoelectrons (p.e.) per GeV per PM (or equivalently 1 p.e./mip/layer/PM) is considered as the minimum required level. This goal was achieved for HAC sections of the prototype calorimeter but not for EMC sections [5] and a considerable effort was devoted to improve the light yield for final modules (see in particular the section 2.3 on WLS).

Since each section is read out on the right (R) and the left (L) side, it is possible to determine the light yield of EMC sections from the electron signal in the following way:

$$\sigma_{pe} = \sigma_{R-L} \ominus \sigma_b = \frac{1}{\sqrt{N_{pe}}}$$

where σ_{pe} is obtained from the width of the R−L distribution normalized by the R+L signal, by subtracting the contribution from the beam size (σ_b) and N_{pe} is the number of photoelectrons (R and L side channels added). The beam size contribution (see fig.35a) can be estimated from the length of the trigger counter B3 and the attenuation λ of the scintillator[1]:

$$\sigma_b = \frac{1}{\sqrt{12}} \frac{d}{\lambda} \sim 1\%$$

This value represents a significant correction to σ_{R-L}:

$$\sigma_{R-L} \sim \frac{8\%}{\sqrt{E}} \sim 2\% \ (E = 15 \ GeV/c)$$

and therefore this method to determine the light yield has a systematic uncertainty of 10 to 20%, as illustrated in fig.35b, where the number of photoelectrons per GeV per PM (averaged over EMC and HAC0 sections of all FCAL modules) is plotted versus σ_b. Fig.36 shows the light yield for all EMC and HAC and HAC0 sections of FCAL modules. The average values for FCAL and RCAL sections are listed in table 7a. We observe that, on the average, more than 100 p.e./GeV/PM have been achieved in FEMC sections, this value representing a considerable improvement as compared to the prototype values (40 p.e./GeV/PM). The expected contribution of p.e. fluctuations to the electron energy resolution is therefore:

$$\sigma_E/E \approx 7\%/\sqrt{E}.$$

[1]We assume a beam spot distributed uniformly over the counter B3

The average light yields per module (EMC and HAC0 sections) are listed in table 7b. The light yield values obtained by this method are compatible with those obtained by other methods (laser and LEDs [18]) which can also be used for HAC1 and HAC2 sections.

5.5 Attenuation length of scintillator

The attenuation length λ of the scintillator has to be known in order to reconstruct the shower position [5]. It was determined by performing for all modules two off-center scans at $\pm$ 6 cm from the middle (see fig.37) with 15 GeV/c electrons. These scans provide two independent measurements of λ for each section:

$$\lambda_1 = -\ 2d_0/\log\rho_1 \quad \text{and} \quad \lambda_2 = -\ 2d_0/\log\rho_2$$

where $\rho_1 = \frac{R_2/R_1}{L_2/L_1}$ and $\rho_2 = \frac{L_3/L_1}{R_3/R_1}$ (see fig.37). The mean values R_1 and L_1 from the central scan are used to normalize the off-center values (R_2, L_2, R_3, L_3) in order to remove possible intercalibration errors between R and L side channels. The values of λ determined in this way are insensitive to horizontal shifts of the beam position (y direction) but can be influenced by vertical shifts (x direction). In order to minimize the error induced by vertical shifts, the average of both λ values has been used:

$$\lambda = \tfrac{1}{2}[\lambda_1 + \lambda_2]$$

In this way the only remaining systematic error is the uncertainty in the exact distance between scan 2 and scan 3 (about 0.3 cm over 12 cm). This systematic error dominates over the statistical error (about 1.5%) and the total uncertainty in λ can be estimated to be 3%.

The values of λ obtained in this way are displayed in fig.38a and 38b for FCAL and RCAL sections, respectively. These figures show systematic differences between the various section types, in particular between FEMC1 (spacer) and FEMC2 (no spacer) sections. The average values per section type are listed in table 8, together with the section-to-section spread which is typically 5 to 6%. Taking into account the uncertainty of 3% in the measurement of λ, we estimate the systematic section-to-section differences to be of the order of 4%. If the same value of λ is used for all sections of a given type, the systematic error in the position measurement in the x direction is therefore:

$$\sigma_x(\lambda) = \frac{D}{\sqrt{12}}\ \frac{\Delta\lambda}{\lambda} \sim 0.2 \text{ cm},$$

D being the section width in the x direction (20 cm). This error is in general negligible compared to the error induced by photoelectron fluctuations (see [5]):

$$\sigma_x(\text{pe}) = \lambda\ \sigma_{R-L} \sim 5 \text{ cm}/\sqrt{E}.$$

5.6 Other results

Energy resolution for electrons. The energy resolution for electrons at 15 GeV/c is 18%/$\sqrt{E}$ for FCAL sections (see fig.39) and 17.8%/$\sqrt{E}$ for RCAL sections. These values are averages over all EMC sections and include the contribution of the beam momentum spread ($\delta p/p \sim 1\%$). If this beam contribution is subtracted, we obtain 17.6%/$\sqrt{E}$ and 17.4%/$\sqrt{E}$

for FCAL and RCAL sections respectively. The sampling fluctuations are of the order of 16%/$\sqrt{E}$ according to Monte Carlo calculations [5], the difference being the contribution of photostatistics (see section 5.4). The section-to-section variations are about 4% and can be almost entirely explained by the 3.5% statistical errors in the determination of the resolution.

Time resolution for electrons. The time resolution measured during the electron energy scan performed with FCAL1 (see section 5.1) is plotted versus beam momentum in fig.40. This result has been obtained by averaging the time measured by R and L side PMs, but the same result holds for R and L side PMs taken separately. This observation suggests that the result is dominated by systematic effects (e.g. the uncertainty in the measurement of the time difference between the trigger and the sampling clock of the electronics). In any case the time resolution of the calorimeter is better than 1 ns above 15 GeV/c. At lower energies the time resolution is dominated by calorimeter noise and by fluctuations in the arrival time of the photoelectrons. For muons in the EMC sections (0.5 GeV equivalent signal) we obtain a time resolution of 3.8 ns which improves by about 10% after averaging over the R and L side.

Noise. The noise for individual channels can be determined with randomly triggered events. In the high gain channels it amounts to about 0.08 pC (8 MeV equivalent energy) for FEMC, 0.10 pC (10 MeV) for REMC and 0.14 pC (13 MeV) for FHAC (0,1,2) and RHAC (0,1) (see fig.41a). This noise is dominated by the fluctuations of the uranium signal. The electronic component, determined by reducing the HV to 400 V, is 0.04 pC (see again fig.41a). The noise in the different calorimeter sections is uncorrelated, but the noise in R and L side channels of the same section is correlated by about 50%, since the main source is the common fluctuations of the uranium signal. For this reason the total noise in a 20×20 cm² FCAL supertower (EMC+HAC1+HAC2) adds up to about 0.45 pC corresponding to 47 MeV (high gain). The low gain, on the contrary, is dominated by electronic noise, as shown in fig.41b. This noise is 0.80 pC per channel, equivalent to 84 MeV.

Uniformity scans. A horizontal uniformity scan with the 15 GeV/c electron beam perpendicular to the calorimeter was performed at the center of module FCAL1. The result is displayed in fig.42a. We observe dips every 5 cm. These dips are due to the gap between scintillator tiles (about 0.5 mm). The drop of the electron signal is about 4%, similar to previous results obtained with the prototype modules [5]. The beam size was determined by the width of trigger counter B3 (6 mm). Additional measurements were performed with a drift chamber in front of the calorimeter. In this case the position of the incident particles can be determined to within 300 μm and the dips increase to about 10%. A similar scan performed at the center of module RCAL1 is shown in fig.42b. We observe again clear dips at module boundaries every 10 cm. At the position of the spacer (y=20 cm in the figure) the signal drops by about 7% as compared to the center of the strip.

6. SUMMARY AND CONCLUSIONS

The 48 modules of the forward (FCAL) and rear (RCAL) ZEUS high resolution uranium-scintillator calorimeter have been constructed. In order to achieve the required energy resolution, position resolution, uniformity of response and at same time a calibration precise

to within 1% from the uranium radioactivity, a strict quality control of the calorimeter components and tolerances has been enforced. Six FCAL and four RCAL modules have been extensively tested in a particle beam at CERN with electrons, muons and hadrons. Most of the elements of the final readout electronics have been used in this test. The main results of this test are summarized below.

- The overall readout with 16.5 bits dynamic range and 10 MHz analog pipeline can be calibrated using charge injection, the signal from the uranium radioactivity and random triggers. The readout electronics achieves a pedestal stability of about 3 MeV and a gain stability of 0.5% over a period of 1 week. The PM gains can be monitored to within 0.5% by measuring the uranium radioactivity every 8 hours.

- The calorimeter response to electrons in the range of 15 to 110 GeV/c is linear within $\pm$ 1% for sections equipped with XP1911 PMs. For sections equipped with R580 PMs a deviation up to 2% at 110 GeV/c is observed.

- A precise determination of the absolute calibration scale of the calorimeter has been possible thanks to a precise measurement of the beam momentum with a spectrometer. This absolute calibration is 9.51 pC/GeV determined with 15 GeV/c electrons incident in EMC sections of FCAL after setting the UNO current in these sections to 100 nA.

- The UNO currents alone provide an intercalibration of the calorimeter sections precise to within 1.1% (1.5% for EMC sections of RCAL). This result is based on 33% and 22% of all FCAL and RCAL channels respectively. The average differences between modules are in general smaller than 1% (0.5% and 0.7% for electrons in FCAL and RCAL respectively). For HAC sections the accuracy of calibration, based on a study of muon and hadron signals, is about 1%. Since this calibration accuracy meets the anticipated goals, no beam calibration is required for the remaining modules.

- The average light yield for FEMC sections is 110 p.e./GeV/PM and for REMC sections 140 p.e./GeV/PM. These values correspond to 1.4 and 1.7 p.e./mip/layer/PM respectively (HAC0 sections included).

- The attenuation length of the scintillator tiles is about 70 cm with some systematic differences between the different section types.

- The energy resolution for 15 GeV/c electrons is on the average $17.6\%/\sqrt{E}$ for FCAL modules and $17.4\%/\sqrt{E}$ for RCAL modules.

' The time resolution for electrons is better than 1 ns above 15 GeV. At lower energies this value degrades due to noise. The result for muons in EMC sections is about 4 ns.

. The noise obtained with random triggers is 0.08, 0.10 and 0.14 pC (or equivalently 8, 10 and 13 MeV) for FEMC, REMC and HAC high gain channels respectively. The noise for a complete FCAL tower including EMC, HAC1 and HAC2 sections is 0.45 pC corresponding to 47 MeV. The noise is dominated by uranium noise in the high gain and by electronic noise in the low gain, where it amounts to 0.80 pC or equivalently 84 MeV per PM channel.

- Nonuniformities for electrons under normal incidence at the boundaries of EMC sections are of the order of 4% for FCAL modules. In the RCAL case the drop in signal is 6% for boundaries with spacer and about 2% for boundaries without spacer.

At present (April 91) all modules of FCAL and RCAL have been transported to DESY, passed a detailed final quality control using movable ^{60}Co sources and cosmic rays and installed into the ZEUS detector.

References

[1] Proceedings of the HERA Workshop, Edited by R.Peccei, 1988.

[2] ZEUS, a Detector for HERA, Letter of Intent, DESY, June 1985,
The ZEUS Detector, Technical Proposal, DESY, March 1986,
The ZEUS Detector, Status Report 1987, DESY, September 1987,
The ZEUS Detector, Status Report 1989, DESY, March 1989.

[3] T.Akesson et al., Nucl. Inst. and Meth.A241(1985)17,
T.Akesson et al., Nucl. Inst. and Meth.A262(1987)243.

[4] B.Anders et al., DESY 86-105 (1986),
G.d'Agostini et al., Nucl. Inst. and Meth.A274(1989)134.

[5] U.Behrens et al., Nucl. Inst. and Meth.A289(1990)115.

[6] A.Andresen et al., Nucl. Inst. and Meth.A290(1990)95.

[7] ZEUS Collaboration, in preparation.

[8] J.Straver et al., ZEUS Notes 86-56, 87-48 and 88-100 (unpublished),
R.Blankers, NIKHEF-H/90-10 (unpublished),
J.Straver, Design, Construction and Beam Tests of the High Resolution Uranium
Scintillator Calorimeter for ZEUS, PhD Thesis, NIKHEF-H(1991).

[9] T.Kamon et al., Nucl. Inst. and Meth.213(83)261.

[10] A.Dannemann et al., High and Low Dose Rate Irradiation of Scintillators and
Wave-Length Shifters, Proceedings of the ECFA/LHC workshop, Aachen,
CERN 90-10 Vol III (1990) 645

[11] J.B.Birks, Proc. Phys. Soc. A64(1951)874.

[12] M.Hirschberg, R.Beckmann, U.Brandenburg, H.Brückmann and K.Wick,
Precise measurement of Birks' kB parameter, in preparation

[13] J.Hartmann et al., Light Guides for the ZEUS Forward and Rear Calorimeters,
submitted to Nucl. Inst. and Meth.A.

[14] R.Blankers et al., NIKHEF-H/90-11 (unpublished).

[15] C.Pegel and H.Prause, Radiation from thick Plates of Depleted Uranium,
Zyklotron-S2/85 (1985), unpublished, and
I.Inst. für Exp.Phys.(Hamburg Univ.), Jahresbericht 1984/85, p.77,
C.M.Lederer and V.S.Shirley, Table of Isotopes, J.Wiley, New York (1978).

[16] B.Anders and H.Brückmann, Radiation Damage from natural DU Radioactivity.
I.Inst. für Exp.Phys.(Hamburg Univ.), Jahresbericht 1984/85, p.75,
P.Plato, Int.Journal of Applied Radiation and Isotopes 33(1979)109,
Coleman, Hudson, Plato, Health Physics 44(1983)395.

[17] ZEUS Collaboration, in preparation.

[18] J.Mitchell et al., Status of the FCAL/RCAL laser calibration system,
ZEUS Note 90-104 (unpublished),
A.Bamberger et al., The laser/LED system for the FCAL/RCAL,
ZEUS Note 90-119 (unpublished).

[19] H.Fawcett, The Effect of Variations in DU Plate Thickness on the Calibration
of the ZEUS FCAL and RCAL, ZEUS Note 91-28 (unpublished).

[20] T.Kawamoto, T.Kobayashi, D.Plane, Field Measurement of
BEND-3 magnet at X5, TKYLEP-40 (1985), unpublished.

[21] W.Sippach et al., Development of the Front End Electronic for the ZEUS
high Resolution Calorimeter, IEEE Trans.Nucl.Sci. NS-36(1989)465,
A.Caldwell et al., Design and Implementation of a high Precision Readout System
for the ZEUS calorimeter, to be published,
L.Hervás, The Pipelined Readout for ZEUS Calorimter, PhD Thesis,
DESY Internal Report F35D-91-01(1991).

[22] H.Boterenbrood et al., The Transputer Readout System of the CERN Test Setup,
ZEUS Note 90-010 (unpublished),
L.W.Wiggers and J.C.Vermeulen, The Use of Transputers in the ZEUS
Online System, Comp.Phys.Comm. 57(1989)316.

[23] J.Brau, T.Gabriel, Nucl. Inst. and Meth.A238(1985)489,
H.Brückmann, Hadron Calorimetry - A Puzzle of Physics, Proc. Workshop
on Compensated Calorimetry, Pasadena (1985) CALT-68-1305,
H.Brückmann et al., DESY 86-155(1986),
R.Wigmans, Nucl. Inst. and Meth.A259(1987) 389.

[24] E.Bernardi, On the Optimization of the Energy Resolution of Hadron Calorimeter,
PhD Thesis, Hamburg Univ., DESY Internal Report F1-87-01(1987).

[25] K.S.Kölbig, B.Schorr, Comp.Phys.Comm. 31(1984)97.

Table 1a Layer structure of EMC calorimeter sections.

material (EMC)	thickness (mm)	thickness (X_0)	thickness (λ)
steel	0.2	0.011	0.0012
DU	3.3	1.000	0.0305
steel	0.2	0.011	0.0012
paper	0.2		
SCI	2.6	0.006	0.0033
paper	0.2		
contingency	0.9		
sum	7.6	1.028	0.0362

effective X_0	0.74 cm
effective λ	21.0 cm
effective Moliere radius	2.02 cm
effective critical energy	10.6 MeV
effective density	8.7 g/cm³

Table 1b Layer structure of HAC calorimeter sections.

material (HAC)	thickness (mm)	thickness (X_0)	thickness (λ)
steel	0.4	0.023	0.0024
DU	3.3	1.000	0.0305
steel	0.4	0.023	0.0024
paper	0.2		
SCI	2.6	0.006	0.0033
paper	0.2		
contingency	0.9		
sum	8.0	1.052	0.0386

effective X_0	0.76 cm
effective λ	20.7 cm
effective Moliere radius	2.00 cm
effective critical energy	12.3 MeV
effective density	8.7 g/cm³

Table 2a FCAL module types and composition.

FCAL module type	F1T*	F1B*	F11	F12	F21	F22	F3	F4	F5	F6
number of modules	1	1	2	2	2	2	2	2	2	2
active height (cm)	220	220	460	460	420	420	380	340	300	220
total weight (T)	5.9	5.9	12.4	12.4	11.3	11.3	9.3	8.8	6.6	4.8
towers (20×20)	11	11	23	23	21	21	19	17	15	11
depth (λ)	7.1	7.1	7.1	7.1	7.1	7.1	6.4	6.4	5.6	5.6
EMC sections (5×20)	36	36	76	68	52	44	36	12	-	-
HAC0 sections (20×20)	2	2	4	6	8	10	10	14	15	11
HAC1 sections (20×20)	11	11	23	23	21	21	19	17	15	11
HAC2 sections (20×20)	11	11	23	23	21	21	19	17	15	11
EMC channels (XP1911)	72	72	152	136	104	88	72	24	-	-
HAC channels (R580)	48	48	100	104	100	104	96	96	90	66

* special modules above and below the beam pipe.

Table 2b RCAL module types and composition.

RCAL module type	R1T*	R1B*	R11	R12	R21	R22	R23	R3	R4	R5	R6
number of modules	1	1	2	2	2	2	2	2	2	2	2
active height (cm)	220	220	460	460	420	420	420	380	340	260	220
total weight (T)	3.3	3.7	7.7	7.7	7.0	7.0	7.0	6.4	5.7	3.7	3.0
towers (20×20)	11	11	23	23	21	21	21	19	17	13	11
depth (λ)	4.0	4.0	4.0	4.0	4.0	4.0	4.0	4.0	4.0	3.3	3.3
EMC sections (10×20)	10	18	38	34	30	26	22	18	6	-	-
HAC0 sections (20×20)	-	2	4	6	6	8	10	10	14	13	11
HAC1 sections (20×20)	11	11	23	23	21	21	21	19	17	13	11
HAC2 sections (20×20)	-	-	-	-	-	-	-	-	-	-	-
EMC channels (R580)	20	36	76	68	60	52	44	36	12	-	-
HAC channels (R580)	22	26	54	58	54	58	62	58	62	52	44

* special modules above and below the beam pipe.

Table 4a The electronics calibration cycle performed for each module.

step	run type	events/run	runs	comment
1	DC	50	2	ADC/V conversion
2	$V_{inj}(0\ V)$	50	58	pipeline cell pedestals
3	$V_{inj}(2\ V)$	50	58	pipeline cell gains
4	V_{inj}	50	8	pipeline cell linearity
5	Q_{inj}	100	2	pulse slopes
6	Q_{inj}	100	8	pulse linearity
7	Q_{inj}	100	2	ground check

Table 4b The 'beam-on' test cycle performed for each module.

scan number	particles	E(GeV/c)	events per run	runs F12(F11)	runs R12(R11)	sensitive sections
1	electrons	15	2000	74(80)	40(42)	EMC(H/L)
2	electrons	100	2000	74(80)	40(42)	EMC(L)
	+ muons		2000			EMC(H)
3	hadrons	100	5000	23	23	HAC(L)
	+ muons		10000			HAC(H)
4	electrons	15	2000	74(80)	40(42)	EMC(H/L)

Table 4c The 'beam-off' calibration cycle performed every 8 hours.

scan number	run type	events per run	runs (FCAL)	runs (RCAL)	comment
1	UNO	1000	7	4	I_{uno} measurement
2	$Q_{inj}(10\ pC)$	1000	7	4	gains for Q_{inj}
3	$Q_{inj}(80\ pC)$	1000	7	4	pedestals for beam
4	Random	1000	7	4	PM monitoring
5	LED(AC)	1000	7	4	PM monitoring
6	LED(DC)	1000	7	4	PM monitoring
7	laser	1000	7	4	PM monitoring

Table 3a Influence of thickness tolerances for EMC sections on the e/UNO ratio.

EMC	f^e	f^{uno}	F	$\Delta t/t$	$\Delta(e/UNO)$
s	+0.93	+0.40	0.21	1.1%	0.2%
u	-0.87	+0.05	0.25	1.9%	0.5%
c	-0.06	-0.99	0.18	1.8%	0.3%
total					0.6%

Table 3b Influence of thickness tolerances for EMC sections on the h/UNO ratio.

EMC	f^h	f^{uno}	F	$\Delta t/t$	$\Delta(h/UNO)$
s	+0.93	+0.40	0.10	1.1%	0.1%
u	-0.87	+0.05	0.18	1.9%	0.3%
c	-0.06	-0.99	0.18	1.8%	0.3%
total					0.4%

Table 3c Influence of thickness tolerances for EMC sections on the μ/UNO ratio.

EMC	f^μ	f^{uno}	F	$\Delta t/t$	$\Delta(\mu/UNO)$
s	+1.00	+0.40	0.12	1.1%	0.1%
u	-	+0.05	0.01	1.9%	0.0%
c	-	-0.99	0.19	1.8%	0.3%
total					0.3%

Table 3d Influence of thickness tolerances for HAC sections on the h/UNO ratio.

HAC	f^h	f^{uno}	F	$\Delta t/t$	$\Delta(h/UNO)$
s	+0.94	+0.53	0.05	2.4%	0.1%
u	-0.82	+0.13	0.11	2.1%	0.2%
c	-0.11	-1.53	0.16	1.3%	0.2%
total					0.3%

Table 3e Influence of thickness tolerances for HAC sections on the μ/UNO ratio.

HAC	f^μ	f^{uno}	F	$\Delta t/t$	$\Delta(\mu/UNO)$
s	+1.00	+0.53	0.05	2.4%	0.1%
u	-	+0.13	0.01	2.1%	0.0%
c	-	-1.53	0.17	1.3%	0.2%
total					0.2%

Table 6a Average charge (in pC) per module in HAC sections.

module	HAC1 muons 100 GeV/c(H)	Δ (%)	HAC1 hadrons 100 GeV/c(L)	Δ (%)	HAC2 muons 100 GeV/c(H)	Δ (%)	HAC2 hadrons 100 GeV/c(L)	Δ (%)
FCAL1	15.33	-0.2	529.0	-2.3	15.79	+1.0	72.0	-3.1
FCAL2	15.77	+1.3	539.4	-0.4	15.90	+1.7	75.9	+2.3
FCAL3	15.57	+0.1	541.2	+0.0	15.54	-0.6	74.7	+0.7
FCAL4	15.44	-0.8	541.9	+0.1	15.53	-0.6	74.3	+0.1
FCAL5	15.57	+0.1	550.1	+1.6	15.50	-0.9	74.0	-0.3
FCAL6	15.46	-0.6	546.6	+1.0	15.58	-0.4	74.5	+0.4
average	15.56		541.1		15.64		74.2	
RCAL1	15.60	-0.1	536.1	+1.2				
RCAL2	15.64	+0.1	529.5	+0.0				
RCAL3	15.53	-0.6	524.1	-1.0				
RCAL4	15.71	+0.6	528.6	-0.2				
average	15.62		529.6					

Table 6b Spread of h/UNO and μ/UNO values in HAC sections.

module	HAC1 muons 100 GeV/c(H)	HAC1 hadrons 100 GeV/c(L)	HAC2 muons 100 GeV/c(H)	HAC2 hadrons 100 GeV/c(L)
stat. error	0.3%	0.5%	0.3%	1.7%
FCAL1	0.4%	1.1%	0.5%	2.4%
FCAL2	0.5%	1.3%	0.7%	3.3%
FCAL3	0.5%	0.8%	0.6%	2.7%
FCAL4	0.5%	1.4%	0.5%	3.4%
FCAL5	0.5%	0.8%	0.6%	2.6%
FCAL6	0.7%	1.1%	0.8%	3.5%
all channels	0.9%	1.7%	1.1%	3.4%
RCAL1	0.6%	1.2%		
RCAL2	0.6%	1.5%		
RCAL3	0.5%	1.1%		
RCAL4	0.6%	1.0%		
all channels	0.7%	1.5%		

Table 5a Average charge (in pC) per module in EMC and HAC0 sections.

module	muons 100 GeV/c(H)	Δ (%)	electrons 15 GeV/c(H)	Δ (%)	electrons 15 GeV/c(L)	Δ (%)	electrons 100 GeV/c(L)	Δ (%)
FCAL1	4.73	-0.2	143.0	+0.3	143.3	+0.4	951.6	+0.0
FCAL2	4.75	+0.2	141.9	-0.4	142.0	-0.5	943.4	-0.9
FCAL3	4.77	+0.6	143.7	+0.8	144.0	+1.0	954.4	+0.3
FCAL4	4.73	-0.2	142.6	+0.1	142.8	+0.1	950.4	-0.1
FCAL5	4.75	+0.2	141.8	-0.5	142.1	-0.4	952.4	+0.0
FCAL6	4.73	-0.2	141.9	-0.3	141.9	-0.5	957.2	+0.6
average	4.74		142.5		142.7		951.6	
RCAL1	4.62	-0.4	139.1	+0.4	139.0	+0.4	954.3	+1.0
RCAL2	4.66	+0.4	138.6	+0.0	138.5	+0.0	943.9	-0.1
RCAL3	4.64	+0.0	139.7	+0.8	139.7	+0.8	949.0	+0.5
RCAL4	4.63	-0.2	137.1	-1.1	137.2	-1.0	930.9	-1.5
average	4.64		138.6		138.6		944.5	

Table 5b Spread of e/UNO and μ/UNO values in EMC and HAC0 sections

module	muons 100 GeV/c(H)	electrons 15 GeV/c(H)	electrons 15 GeV/c(L)	electrons 100 GeV/c(L)
stat. error	0.5%	0.3%	0.3%	0.1%
FCAL1	1.3%	1.1%	1.2%	1.0%
FCAL2	1.4%	0.7%	1.1%	1.0%
FCAL3	0.9%	1.2%	1.2%	1.3%
FCAL4	0.8%	0.8%	0.8%	1.0%
FCAL5	1.1%	0.9%	0.9%	0.9%
FCAL6	1.1%	1.0%	1.3%	1.1%
all channels	1.2%	1.1%	1.2%	1.1%
RCAL1	1.1%	1.4%	1.4%	1.7%
RCAL2	0.8%	1.1%	1.1%	0.9%
RCAL3	0.9%	1.1%	1.1%	1.4%
RCAL4	0.9%	1.5%	1.5%	1.2%
all channels	1.0%	1.5%	1.5%	1.6%

Fig.1 Longitudinal cut of the ZEUS central detectors along the beam axis. The three components of the uranium scintillator calorimeter (FCAL, BCAL, RCAL) are shown. The lines indicate the segmentation of the readout.

Fig.2 a) FCAL and b) RCAL front views. The lines indicate the segmentation of the readout.

Fig.3 View of a maximum size FCAL module.

Fig.4 a) Sketch of a C-frame for FCAL module of maximum size and b) sketch of the back beam.

Fig.5 Thickness distributions of DU plates for a) EMC sections from FCAL, b) HAC1 sections from FCAL, c) HAC2 sections from FCAL, d) EMC sections from RCAL and e) HAC sections from RCAL.

Fig.6 Detail of a stack showing DU plates with end pieces, scintillator tiles and spacers (HAC section).

Fig.7 a) Longitudinal cut of a stack from an FCAL module, showing EMC, HAC1, HAC2 sections and the WLS arrangement and b) detail of the back beam showing WLS plates, source tubes, optical fibers, straps and PM housings.

Fig.8 Attenuation length of scintillator pieces (SCSN-38) obtained from the pulse height 30 cm and 89 cm from the PM, with thickness of a) 5 mm and b) 2.6 mm, exposed to DU radioactivity as a function of exposure time. For comparison, the attenuation length of an identical non-irradiated sample is shown.

Fig.9 Scintillator tiles for FCAL sections showing the transverse dimensions.

Fig.10 Thickness distributions for samples of scintillator tiles belonging to a) EMC, b) HAC0, c) HAC1 and d) HAC2 sections of FCAL.

Fig.11 a) Black pattern printed onto the scintillator wrapping paper used to correct the non-uniformities of an EMC scintillator tile, b) uniformity of an EMC scintillator tile before correction and c) uniformity of an EMC scintillator tile after correction. Given is the light yield normalized in the center (x = 90 mm, y = 25 mm).

Fig.12 a) Schematic view of the WLS readout and b) mechanical assembly of the different components (dimension in mm).

Fig.13 Uniformity of a FHAC1 WLS plate, as measured with a xenon lamp, a) before correction and b) after correction.

Fig.14 a) Light yield distribution from a sample of WLS plates for EMC sections of FCAL. b) Maximum non-uniformity measured for a sample of WLS plates from EMC sections of FCAL.

Fig.15 Dark current distribution a) for a sample of XP1911 PMs and b) for a sample of R850 PMs.

Fig.16 a) Schematic view of the stacking robot used at NIKHEF. b) Height deviation from

Table 7a Light yield per section (average over all modules).

component	section	pe/GeV/PM
FCAL	HAC0	227
	EMC	107
	HAC1	-
	HAC2	-
RCAL	HAC0	317
	EMC	139
	HAC1	-

Table 7b Light yield per module (only EMC and HAC0 sections).

component	module	pe/GeV/PM
FCAL	FCAL1	86
	FCAL2	117
	FCAL3	118
	FCAL4	119
	FCAL5	124
	FCAL6	131
RCAL	RCAL1	184
	RCAL2	160
	RCAL3	157
	RCAL4	145

Table 8 Attenuation length of scintillator per section.

component	section	λ (cm)	r.m.s.
FCAL	HAC0	73.9	4.5%
	EMC1	66.2	6.8%
	EMC2	70.7	5.2%
	HAC1	-	-
	HAC2	-	-
RCAL	HAC0	75.6	7.9%
	EMC1	69.6	4.3%
	HAC1	-	-

Fig. 2a FCAL front view

Fig. 2b RCAL front view
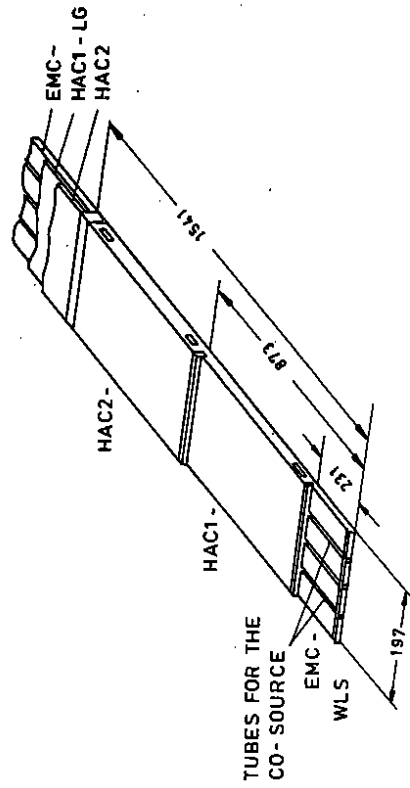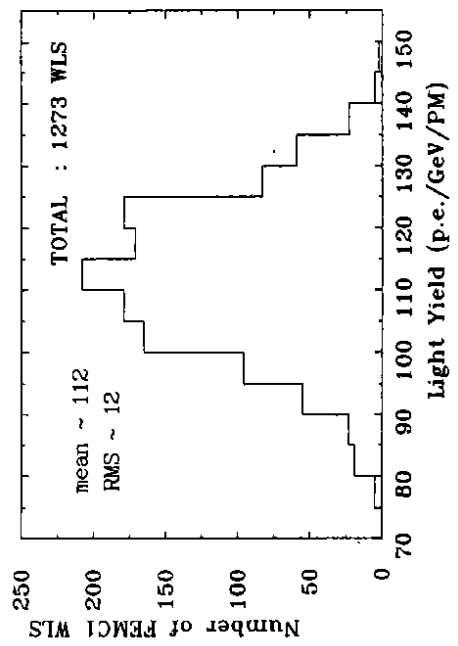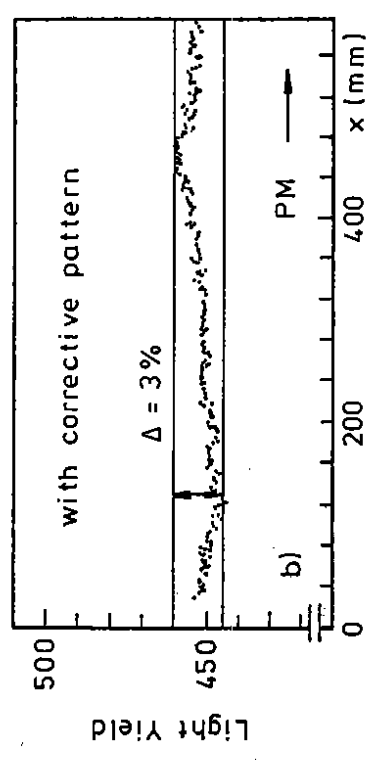

Fig. 1

Fig. 4a

Fig. 4b

Fig. 3

FEMC

mean ~ 3.284
rms ~ 1.9 %

Thickness (mm)

Fig. 5a

REMC

mean ~ 3.315
rms ~ 1.9 %

Thickness (mm)

Fig. 5d

FHAC1

mean ~ 3.281
rms ~ 2.1 %

Thickness (mm)

Fig. 5b

RHAC

mean ~ 3.318
rms ~ 1.9 %

Thickness (mm)

Fig. 5e

FHAC2

mean ~ 3.279
rms ~ 2.3 %

Thickness (mm)

Fig. 5c

Fig. 6

Fig. 8a

Scintillator dimension :
80 × 5 × 0.50 cm³
● irradiated sample
○ non-irradiated sample

Λ (cm)
115
110
105
100
95
90

Time (d)
0   500   1000

Fig. 8b

Scintillator dimension :
80 × 5 × 0.26 cm³
● irradiated sample
○ non-irradiated sample

Λ (cm)
80
78
76
74
72
70

Time (d)
0   500   1000

Fig. 7a

FEMC/FHAC0
FHAC1
FHAC2

W.L.S. FEMC/FHAC 0
W.L.S. FHAC 1
L.G. FEMC/FHAC 0
L.G. FHAC 1
L.G. FHAC 2
W.L.S. FHAC 2

Fig. 7b

12
13
14
15
SOURCE TUBE
LIGHT FIBRE

FHAC1
mean ~ 2.583
rms ~ 2.4 %

Thickness (mm)

Fig.10c

FHAC2
mean ~ 2.582
rms ~ 2.5 %

Thickness (mm)

Fig.10d

FEMC
mean ~ 2.584
rms ~ 1.1 %

Thickness (mm)

Fig.10a

FHAC0
mean ~ 2.584
rms ~ 1.2 %

Thickness (mm)

Fig.10b

EMC   191   49,3   47,1   9,8   199,2

HAC 1   186   13,8   197   199,2

HAC 2   181   13,8   197   199,2

Fig. 9

Fig. 11a

191 mm

50 mm

Fig. 11b

45	0.989	0.981	0.984	0.984	0.970	0.981	0.994	0.979
	1.035	1.012	1.000	0.996	0.991	0.993	0.988	0.994
35	1.113	1.075	1.025	0.993	1.000	1.013	1.004	1.006
	1.111	1.100	1.050	1.009	1.013	1.009	1.005	0.997
	1.133	1.096	1.087	1.015	1.016	1.010	1.004	1.000
25	1.142	1.108	1.070	1.027	1.029	1.009	1.009	1.000
	1.136	1.101	1.076	1.036	1.024	1.019	1.007	1.000
15	1.126	1.109	1.071	1.037	1.030	1.018	1.003	0.999
			1.045	1.025	1.013	1.006	0.995	0.993
	1.100	1.080	1.064	1.036		0.990	0.990	0.972
5	1.109	1.086	1.061	1.050	1.019	0.991	0.986	0.974
	10	30	50	70	90 (mm)			

Fig. 11b

Fig. 11c

45	0.960	0.972	0.972	0.985	0.996	0.989	0.996	0.985
	0.973	0.964	0.968	0.985	0.990	0.997	0.998	0.996
35	0.980	0.995	0.975	0.965	0.978	1.006	0.999	1.002	0.995
	0.982	1.006	0.994	0.977	0.989	1.005	1.002	1.001	1.004
	0.980	1.020	0.996	0.990	0.987	1.001	1.009	1.001	1.004
25	0.974	1.005	0.996	0.991	0.995	1.013	1.012	1.010	1.000
15	0.972	0.995	0.993	0.987	0.996	1.000	1.006	1.002	0.998
	0.960	0.989	0.983	0.976	0.991	0.998	0.990	0.984	0.989
5	0.937	0.966	0.971	0.970	0.988	0.988	0.979	0.986	0.975
	15	35	55	75	95 (mm)			

--- nonuniformity < 2.5 %
— nonuniformity < 5.0 %

Fig. 11c

Fig. 12a

back reflector

WLS

end reflector

first scintillator

DU-plate

last scintillator

PM

Fig. 12a

Fig. 12b

EMC-
HAC1-LG
HAC2

HAC2-

HAC1-

TUBES FOR THE CO-SOURCE

EMC-

WLS

1541

873

231

197
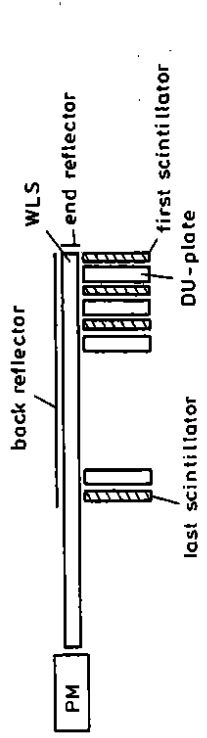
Fig. 12b

Fig 14a

Fig.14b

Fig. 13

Fig. 16a

Fig. 16b

Fig.15a

Fig.15b

B5

calorimeter

B4

B1 B2 B3

beam →
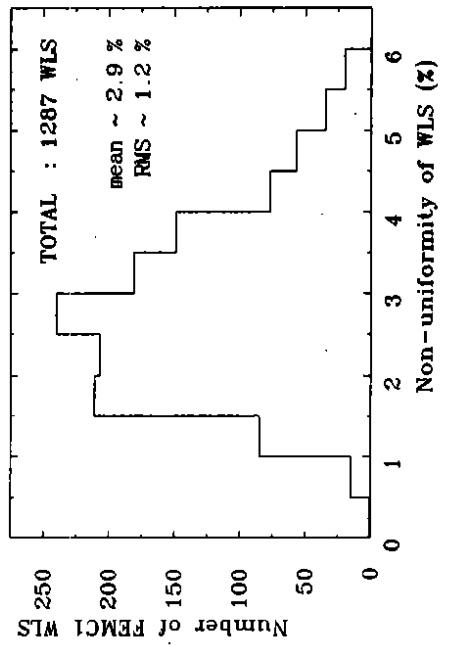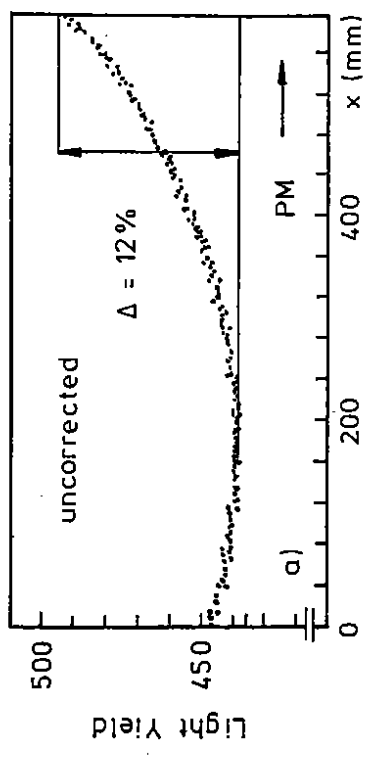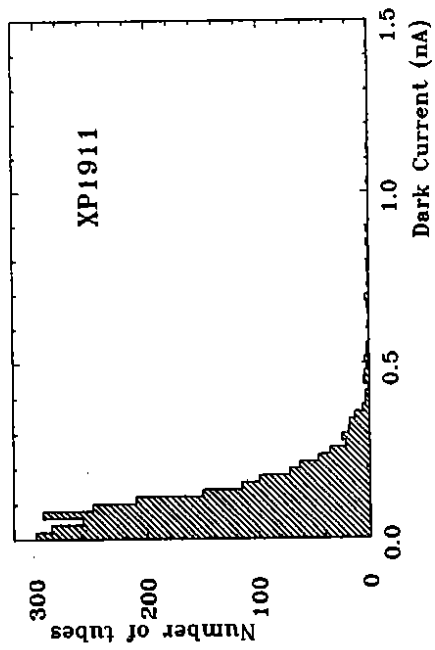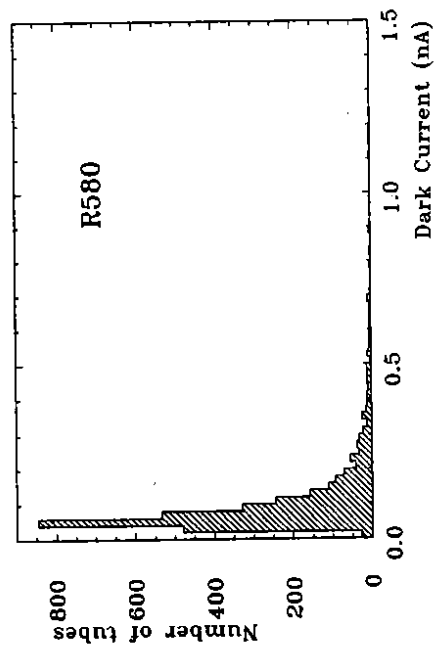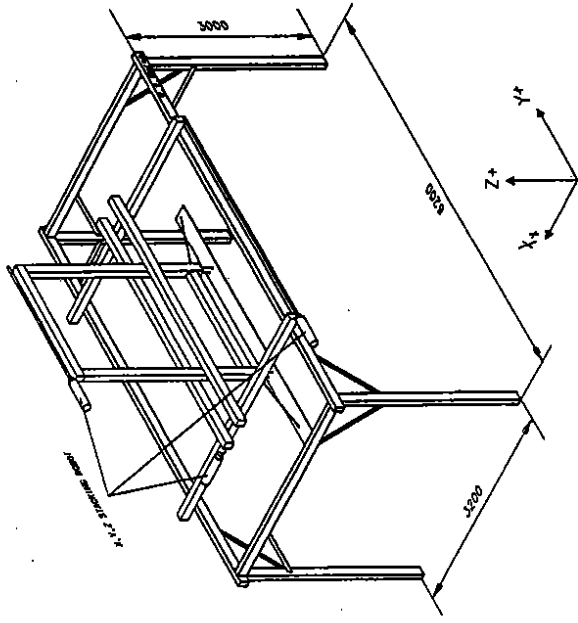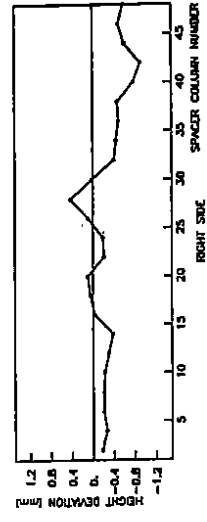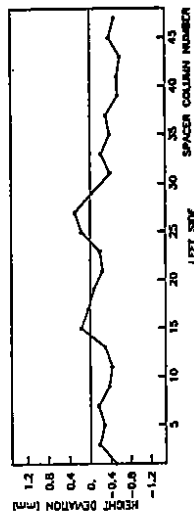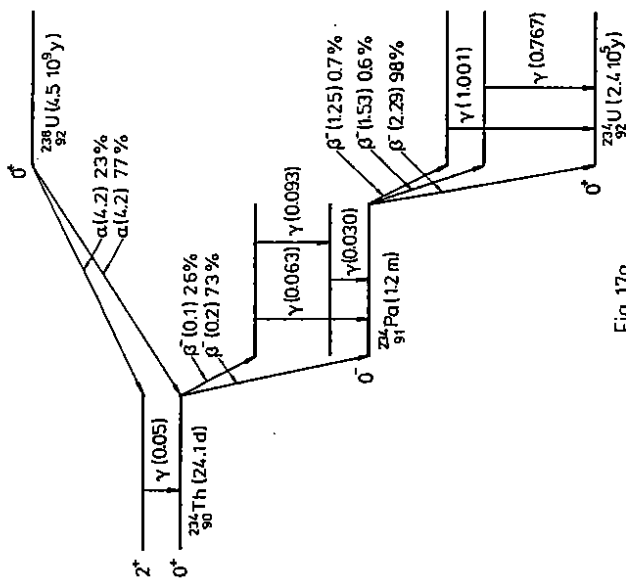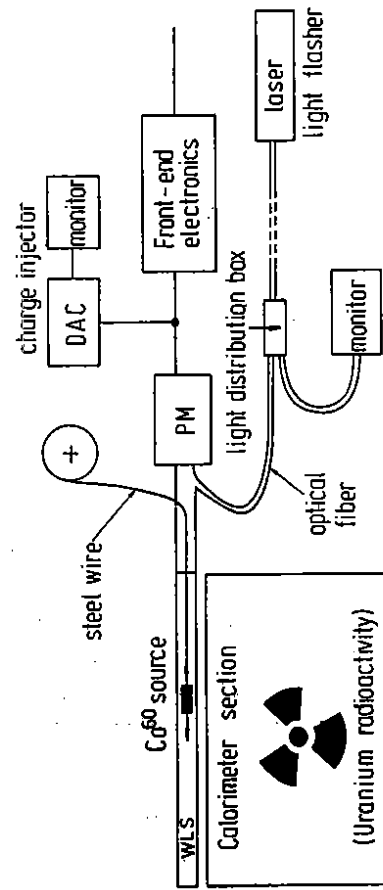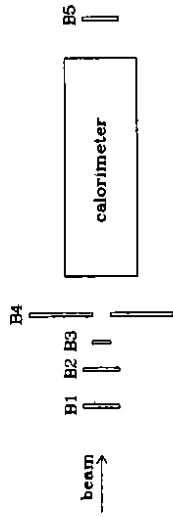
Trigger = B1•B2•B3•B4

Fig. 18a

Fig. 18b

CERENKOV
COUNTERS

COLLIMATOR 1
(horizontal)

MWPC's

BEND 2

Pb-absorber

Q3
COLLIMATOR 2
(vertical)

Q4 Q5

BEND 1

Q1 Q2

HORIZONTAL PLANE

VERTICAL PLANE

8
6
4
2
0
-2
-4
-6
-8

cm

TO
TARGET

0   50   100   150
meters

Fig. 17a

$^{238}_{92}U$ (4.5 10^9y)

2⁺

0⁺

γ (0.05)

$^{234}_{90}Th$ (24.1 d)

α(4.2) 23%
α(4.2) 77%

β⁻(0.1) 26%
β⁻(0.2) 73%

γ(0.063)

γ(0.093)

γ(0.030)

$^{234}_{91}Pa$ (1.2 m)

0⁻

β⁻(1.25) 0.7%
β⁻(1.53) 0.6%
β⁻(2.29) 98%

γ(1.001)

γ(0.767)

$^{234}_{92}U$ (2.4 10^5y)

0⁺

Fig. 17b

charge injector

monitor

DAC

Front-end
electronics

PM

light distribution box

laser
light flasher

monitor

optical
fiber

steel wire

Co⁶⁰ source

Calorimeter section

WLS

(Uranium radioactivity)

beam
->

module

CW base
PM

F.E.
card

HV
controller

Motorola
68020

Slow control

MUX

VME crates

ADC card

Transputers

μVAX

main DAQ

tape

Fig. 19a

Fig. 19b

BEAM

TCAL

0.5°

5m

Fig. 19b

Collimator
7.305 m
6.918 m
bend plane
6.918 m
7.270 m

MWPC1

beam

MWPC2

θ

MWPC3

MWPC4

Fig. 18c

Fig. 18d

Ptrue/Pnominal

1.02

1.01

1.00

0.99

0.98

0   20   40   60   80   100   120

Pbeam (GeV/c)

Fig. 18d

FEMC section

Source signal / UNO signal

Source position (mm)

Fig.21a

FHAC section

Source signal / UNO signal

Source position (mm)

Fig.21b

96 ns

Fig.20a

Fig.20b

Fig.23a

T_c (ns)

Q (%)

Fig.23b

T (ns)

T_c (ns)

Fig.22a

X (cm)

center of tower 12

Q (pC)

Fig.22b

Y (cm)

Boundary between sections 2 and 3

EMC section 3
(tower 12)

EMC section 2
(tower 12)

Q (pC)

Fig.25

Fig.24a

Fig.24b

Fig.27a

Fig.27b

Fig.26a

Fig.26b

H/L gain ratio
FCAL modules
$\sigma = 0.7\%$

Channels

H gain/L gain

Fig.29a

H/L gain ratio
RCAL modules
$\sigma = 0.2\%$

Channels

H gain/L gain

Fig.29b

Events

Electron signal (pC)

Fig.28a

FEMC

Events

Muon signal (pC)

Fig.28b

FHAC1

Events

10000

7500

5000

2500

0

0   20   40   60   80

Muon signal (pC)

Fig.31a

FHAC2

Events

10000

7500

5000

2500

0

0   20   40   60   80

Muon signal (pC)

Fig.31b

Sections

70.0

60.0

50.0

40.0

30.0

20.0

10.0

0.0

e/UNO

FCAL modules

$\sigma = 1.1\%$

110.0   120.0   130.0   140.0   150.0   160.0

Electron signal (R+L) (pC)

Fig.30a

Sections

20.0

15.0

10.0

5.0

0.0

e/UNO

RCAL modules

$\sigma = 1.5\%$

110.0   120.0   130.0   140.0   150.0   160.0

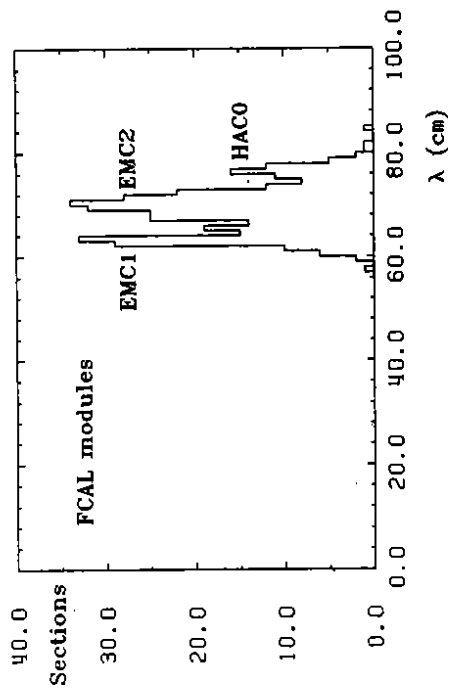Electron signal (R+L) (pC)

Fig.30b

Fig.33a

Fig.33b

Fig.32a

Fig.32b

Fig. 35a

Fig. 35b

Fig. 34a

Fig. 34b

Fig.38a

FCAL modules

Sections

EMC1 EMC2 HAC0

λ (cm)

Fig.38b

RCAL modules

Sections

EMC HAC0

λ (cm)

Fig.36

Light yield
FCAL modules
mean= 116 p.e./GeV/PM

Sections

p.e./GeV/PM

Fig.37

L side

R side

8cm
6cm

x
y

Energy resolution

FCAL modules

mean= 18%/√E

Sections

100
80
60
40
20
0

$(\sigma/E)\sqrt{p}$ (%)

0   5   10   15   20   25

Fig.39

Time resolution

σ_t (ns)

2.0
1.5
1.0
0.5
0.0

Pbeam (GeV/c)

0   20   40   60   80   100   120

Fig.40

HAC

EMC

400 V

σ (pC)

0.20
0.15
0.10
0.05
0.0

Channel number

0.0   50.0   100.0   150.0   200.0   250.0   300.0

Fig.41a

HAC
EMC
400 V

σ (pC)

1.2
1.0
0.8
0.6
0.4
0.2
0.0

Channel number

0.0   50.0   100.0   150.0   200.0   250.0   300.0

Fig.41b

Uniformity scan
FCAL EMC sections

Fig.42a

Uniformity scan
RCAL EMC sections

Fig.42b